CIRCULATION AT THE SOUTH-WEST INDIAN RIDGE IN A HIGH-RESOLUTION GLOBAL OCEAN MODEL

JONATHAN V. DURGADOO.

Dissertation presented for the degree of Masters of Science.

Department of Oceanography, University of Cape Town.

MAY 2008.

ABSTRACT.

The South-West Indian Ridge (SWIR) in the Indian sector of the Southern Ocean is a region where disturbances in the mean flow of the Antarctic Circumpolar Current have been acknowledged to be important in sustaining the marine ecosystem of the Prince Edward Islands. Eddies shed at the ridge travel in a north-eastern direction past the islands. In doing so, these features may also have climatic importance by providing a mechanism for meridional heat and salt exchange in that region. Eddies at the SWIR have been extensively studied over the last decade using hydrographic, satellite, drifter and float data. Numerous processes pertaining to these eddies require comprehensive and frequent monitoring, which is logistically impossible to undertake hydrographically. Therefore, it has become necessary to simulate eddies at the ridge with an appropriate model. This study explores the use of the $^{1}/_{4}^{o}$ and the $^{1}/_{12}^{o}$ Ocean Circulation and Climate Advanced Modelling (OCCAM) project. The model's representation of the dynamic nature of this region is assessed. On average 2 – 3 intense and well-defined eddies are generated per year within the model; having mean longevities of 4.89 ± 2.20 months with average advection speeds of 5.51 ± 1.57 km day^{-1}. The model generates fewer warm eddies than anticipated. Most simulated eddies reach their peak intensity within 1.5 – 2.5 months after genesis, with their depths reaching 2000 – 3000 m. Thereafter they dissipate within approximately 3 months. The decay of eddies is characterised by a decrease in their sea surface height signature, a weakening in their rotation rates and by the modification of their temperature-salinity characteristics. Overall, it can be concluded that the dynamics at the SWIR is well simulated by OCCAM suggesting a number of ways in which this model can be used in the future to study the mesoscale processes in this region.

TABLE OF CONTENTS.

1. INTRODUCTION.

The quasi-permanent band of low pressure around the Antarctic continent and the band of high pressure in the subtropics work in synergy to produce strong westerly geostrophic winds over the Southern Ocean. The curl of the wind stress drives the eastward flowing Antarctic Circumpolar Current (ACC), which is part of the deep transport of the global conveyor belt. It carries approximately 134 ± 13 Sv of polar and subpolar water masses through the Drake Passage (Whitworth, 1983; Nowlin and Klinck, 1986) and 160 Sv south of Africa (Park *et al.*, 2001).

The ACC is concentrated at frontal bands (Figure 1.1), a direct consequence of the wind regime prevailing over the Southern Ocean (Orsi *et al.*, 1995; Belkin and Gordon, 1996). To the north, the Subtropical Convergence (STC) separates the warm sub-tropical gyres from the subantarctic regime. The Subantarctic Front (SAF) demarcates the northern boundary of the Antarctic Polar Frontal Zone. With a weaker surface temperature expression, the SAF is usually identified at the subsurface, typically at 200 m. The Antarctic Polar Front (APF) marks the southern boundary of the Antarctic Polar Frontal Zone and the beginning of the Antarctic Zone. Bottom topography and prevailing westerly winds, in tandem, play a major role in the temporal and spatial variability in the flow in the Antarctic Polar Frontal Zone throughout the Southern Ocean (Nowlin and Klinck, 1986; Park et al., 1993). The main core of the ACC is commonly associated with the SAF and APF (Rintoul and Sokolov, 2001; Budillion and Rintoul, 2003). South of the African continent, based on 89 hydrographic sections, the STC, SAF and APF are located on average at 41.6 ± 1.07 °S, 46.4 ± 1.07 °S and 50.3 ± 1.33 °S respectively (Lutjeharms and Valentine, 1984).

In addition to showing the global position of the major Southern Ocean fronts, Figure 1.1 depicts the spacial variability of the frontal systems and their fragmentations. Upon encountering prominent topographic features, the ACC is deflected equatorward and subsequently poleward so as to conserve potential vorticity. South of Africa (Figure 1.2), in the vicinity of the South-West Indian Ridge, the SAF and APF show very stochastic

behaviour. Read and Pollard (1993) have reported only one major intense front at 33°E. Earlier studies, however, gave the SAF and APF at distinct latitudes (Lutjcharms and Valentine, 1984). Having found two branches of the SAF in their section at 30°E, Park *et al.* (2001) have scrutinized Read and Pollard's results finding two expressions of the APF. The discrepancy was attributed to a possible cold eddy inducing a meandering in

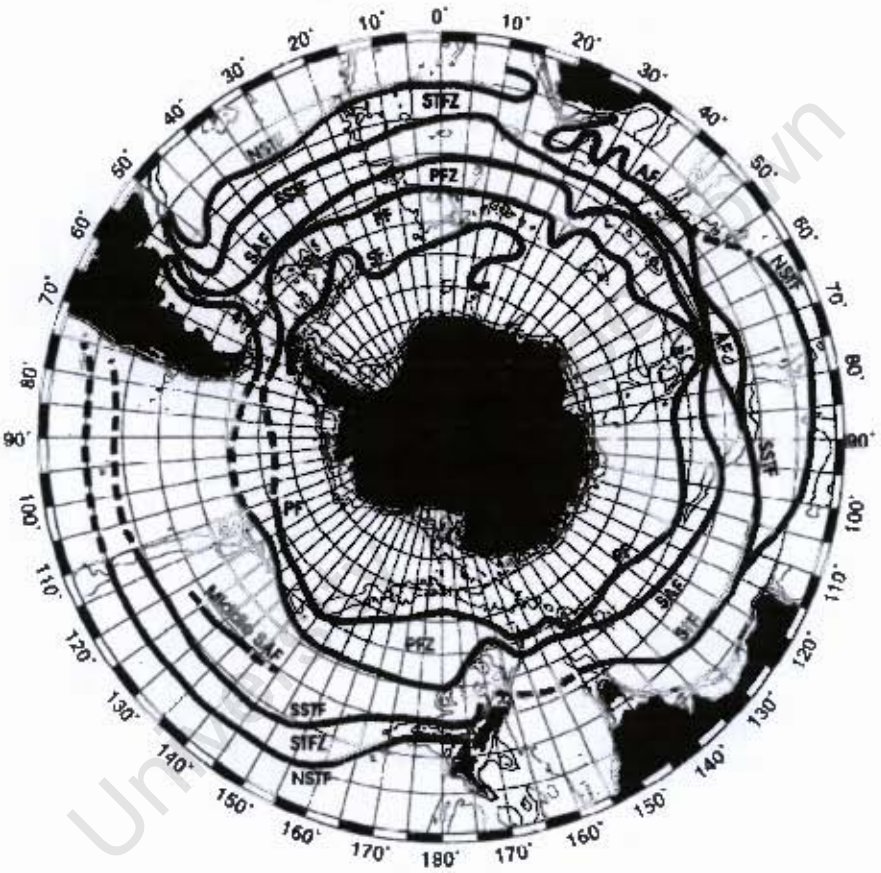

Figure 1.1: Geographic position of the Southern Ocean fronts namely: AF – Agulhas Front, STF – Subtropical Convergence, SAF – Subantarctic Front, PF – Antarctic Polar Front and SF – Scotia Front with prefixes N – Northern and S – Southern. Inter-frontal zones are also demarcated: STFZ – Subtropical Frontal Zone and PFZ – Antarctic Polar Frontal Zone. (Belkin and Gordon 1996).

the front. Clear of the South-West Indian Ridge, the ACC breaks up into multiple fragments (Holliday and Read, 1998; Pollard and Read, 2001). Kostianoy *et al.* (2004), using satellite sea surface temperature data (1997 – 1999), have mapped the fronts in the Indian sector of the Southern Ocean. In the western part (20 – 60°E), their results depict the latitudinal variability of the SAF and APF as well as giving a clear indication of their

temporal variability and fragmentation. The Prince Edward Islands are found in this highly unpredictable environment.

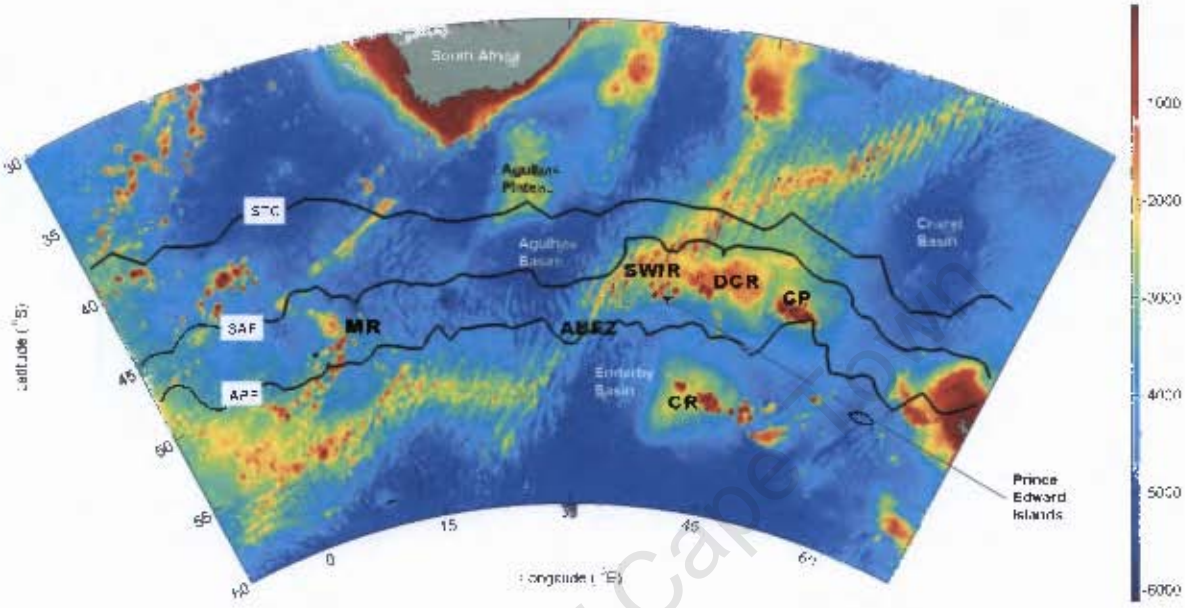

Figure 1.2: Bottom topography (in meters) of the African sector of the Southern Ocean south of 30°S used in OCCAM at $^{1}/_{12}^{\circ}$ resolution. The South-West Indian Ridge (SWIR) is intersected by a series of fractures with the Andrew Bain Fracture Zone (ABFZ) being the most extensive. Other notable bathymetric features referred to in the text are the Conrad Rise (CR), the Del Caño Rise (DCR), the Crozet Plateau (CP) and the Meteor Rise (MR). The average position of the three major fronts associated with the ACC is also shown: the Subtropical Convergence (STC), the Subantarctic Front (SAF) and the Antarctic Polar Front (APF).

This island group consists of Marion Island and Prince Edward Island, the former being the largest. The islands, of volcanic origin, rise to prominence above the South-West Indian Ridge (SWIR) at 46.7°S, 37.7°E. The ridge separates the African plate from the Antarctic plate and is intersected by a series of composite deep fractures (Figure 1.2). The Andrew Bain Fracture Zone centred at 50°S, 30°E is of particular importance because of its direct influence on the eastward-flowing ACC (Ansorge and Lutjeharms, 2003), channelling approximately 110 ± 10 Sv of the current (Pollard and Read, 2001). Over the last two decades, research around the Prince Edward Islands and the general area surrounding the South-West Indian Ridge has been undertaken primarily by South African scientists.

2. RESEARCH REVIEW.

Surveys around the South-West Indian Ridge prior to 1989 were sparse with most studies undertaken in the direct vicinity of the Prince Edward Islands, where an enhanced marine productivity was observed (Allanson *et al.*, 1985; Duncombe Rae 1989a,b,c; Perissinotto and Boden, 1989; Perissinotto *et al.*, 1990). A few transects revealed the position of the Southern Ocean fronts with respect to the location of the islands (Lutjeharms and Valentine, 1984; Lutjeharms, 1985; Duncombe Rae, 1989a,b; Lutjeharms, 1990). The structure of the ACC in that region was known and the temporal and spatial variability of the fronts were acknowledged (Park et al., 1993; Ansorge *et al.*, 1999; Read and Pollard, 1993).

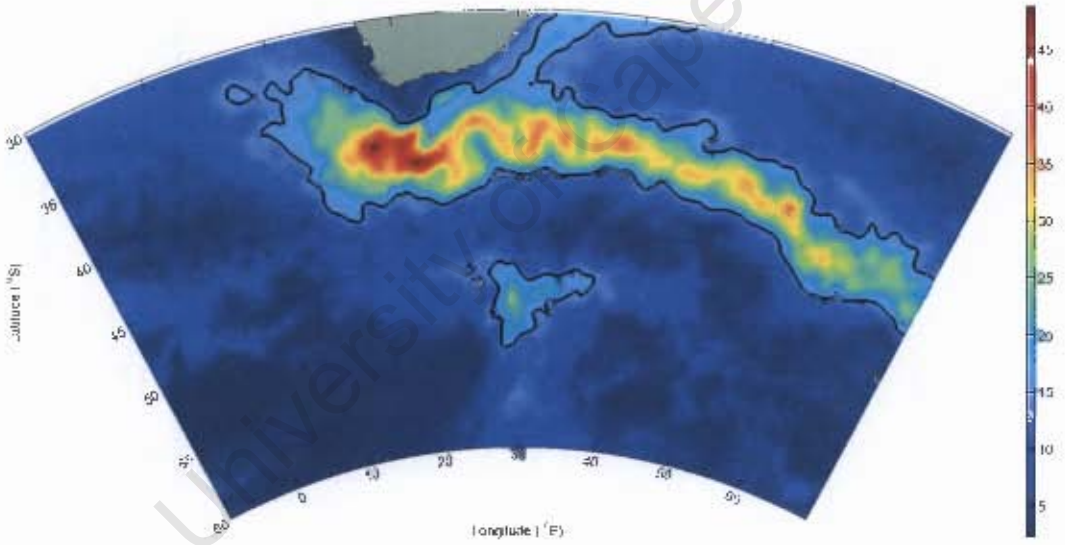

Figure 2.1: The root-mean-square (rms.) in Sea Level Anomaly (cm) calculated from a 13-year record of altimetry products. Two broad regions of variability (demarcated by the 15 cm contour) are observed in the African sector of the Southern Ocean: the Agulhas regime (comprising the Agulhas Current, the Agulhas retroflection, the Agulhas Return Current and the Subtropical Convergence) and at the South-West Indian Ridge.

Various hypotheses have been put forward to explain the enhanced biological productivity observed in close proximity of the islands (Ansorge and Lutjeharms, 2000; McQuaid and Froneman, 2004). Boden (1988) has suggested an 'island mass effect' where nutrient-rich runoff from the islands is contained between Marion and Prince Edward and thus sustains an abundant biota. The Von Kàrmàn vortex street theory,

whereby persistent swirls are observed due to the unsteady separation of the ACC by the islands, was also proposed (Allanson *et al.*, 1985). Later surveys revealed the presence of an anti-cyclonic eddy between the islands favouring retention of nutrients in a suggested Taylor column (Duncombe Rae, 1989b; Perissinotto and Duncombe Rae, 1990; Perissinotto *et al.*, 1990).

2.1. The South-West Indian Ridge Region.

The second Marion Offshore Ecological Survey (MOES-II), undertaken in April 1989, was an attempt to resolve the conundrum. MOES-II provided the first quasi-synoptic view of the general environment around the Prince Edward Islands both up and down stream (46 – 47.5°S; 37.5 – 40.5°E). Results from the survey confirmed the meandering behaviour of the SAF (Ansorge *et al.*, 1999). A sharp deflection of the front north-eastward close to the islands was observed. Furthermore, it was established that the oceanographic conditions upstream of the islands were different to those downstream (Perissinotto *et al.*, 2000). A warm eddy, resulting from the meandering SAF, was observed downstream of the islands.

A repeat survey, the Marion Island Oceanographic Survey II (MIOS-II), was carried out 8 years later covering an even wider geographic region (46 – 48°S; 36 – 42°E). The oceanographic conditions were different from MOES-II. In the western side of the survey area the SAF was intensified, deflecting north-eastward on approaching the islands. Further downstream, two branches of the SAF were observed (Ansorge and Lutjeharms, 2002). However, amidst the meandering SAF, eddies were still present downstream of the islands. These recurring eddy activities triggered much interest, especially with respect to the meridional exchanges of water masses and associated plankton activities. The enhanced biological activity observed in the direct vicinity of the islands was found to be closely related to these eddies (Ansorge *et al.*, 1998; Froneman *et al.*, 1999; Pakhomov *et al.*, 1998, 2000a,b; Ansorge and Lutjeharms, 2002). Water masses entrained in these eddies were either of sub-tropical/sub-antarctic (for warm eddies) or antarctic (for cold eddies) origin, thereby raising questions about the earlier conjectures.

Satellite altimetry provided evidence that the SWIR region was one of high mesoscale variability (Figure 2.1) with the Prince Edward Islands lying in the northern border of that region (Ansorge and Lutjeharms, 2003). An attempt to correlate Sea Surface Height Anomaly (SSHA) to Sea Surface Temperature in that region was made (Ansorge and Lutjeharms, 2000, 2003). Positive anti-clockwise (southern hemisphere) anomalies were found to correspond closely to warm eddies, while negative clockwise anomalies corresponded to cold eddies. Because of the inherent advantage of satellite remote sensing to provide a continuous dataset, it was possible to look at the trajectories and decay of the anomalies as well as determining their origin. The anomalies were found to be generated at the SWIR, roughly centred at 50°S, 30°E, corresponding to the axial position of the Andrew Bain Fracture Zone (Figure 1.2). Once formed, these eddies were observed to follow a north-eastward direction, along the eastern flank of the ridge until about 47°S where they drift pass the islands. Thereafter, the anomalies are in the final stage of decay and move eastwards in the Enderby Basin. An eddy corridor was empirically defined between 48 – 49°S and 34 – 38°E (Ansorge and Lutjeharms, 2003). Intense anomalies (eddies) were characterised having SSHA > +30 cm (or < -30 cm) (Ansorge and Lutjeharms, 2003, 2005; Pakhomov *et al.*, 2003). However, comprehensive hydrographic data were not available to make any significant posit. Nonetheless, it was clear that eddies observed during MOES-II and MIOS-II were present not only as a result of the islands' interaction with the ACC, but also because of the complex dynamics between the frontal systems and the regional bathymetry.

The need to hydrographically validate results obtained from satellite altimetry was the next logical step. The Dynamics of Eddy Impact on Marion's ECosystem (DEIMEC) programme started in 2002 with the aim to characterise these eddies. Under the programme, four surveys were undertaken (2002 – 2005) during austral autumn (April/May) on board the South African supply vessel, the MV SA Agulhas. The physical setting of the SWIR region as well as its biological community distribution were investigated with transects consisting of alternating CTD (Conductivity-Temperature-Depth) and XBT (eXpendable Bathy-Thermograph) stations with chlorophyll_a measurements taken at every CTD station (Figure 2.2). Drifters and floats were deployed

at strategic position within eddies. Bongo and WP-2 nets, RMT-8 trawls and bottom dredges were also used to study the zooplankton community structure, complementing the physical description of the extended environment around the islands.

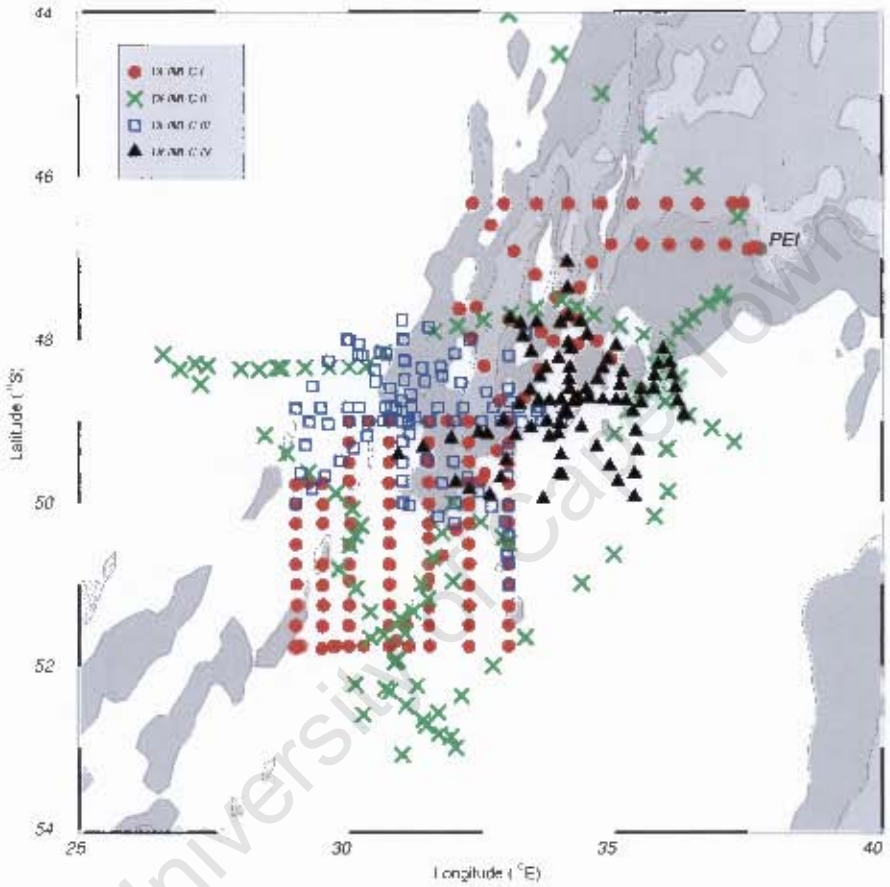

Figure 2.2: The distribution of hydrographic stations from the four DEIMEC surveys undertaken during April/May 2002 – 2005. Bathymetric contours (< 4000 m) show the location of the stations with respect to the SWIR. PEI – Prince Edward Islands.

The first DEIMEC cruise served to survey the area around the ridge, focussing on the Andrew Bain Fracture Zone. Two frontal features were encountered, the southern branch of the SAF and the APF. The former exhibited a high degree of meandering while the latter was concentrated within a narrow band at 51°S. More importantly, it was established that the fracture zone constricted the flow of the ACC acting as a choke point (Froneman *et al.*, 2002). A rich mesozooplankton community structure was also observed in the region, particularly close to the APF (Bernard and Froneman, 2003). At that stage, the main objective to hydrographically characterise the sea surface height anomalies at

their source region and their decay still remained unaddressed. At best, DEIMEC-I provided further evidence of the dynamic and variable nature of the ACC in that region and the direct impact this has on the biology.

Prior to the DEIMEC-II cruise, altimetric products were used to locate three potential sea surface height anomalies near the ridge. The survey was then set up to investigate these anomalies. The anomalies were all found to coincide with eddies confirming earlier hypothesis (Pakhomov *et al.*, 2003). Water masses at the core of these features were characteristic of either Sub-Antarctic Surface Water (SASW) or Antarctic Surface Water (AASW). Two positive anti-clockwise SSHA were associated with relatively warmer SASW while the negative clockwise SSHA entrained fresher and colder AASW. Of the two warm eddies, the one closer to the islands had a weaker T/S signature, giving an indication of the decay of the feature. Moreover, the APF was found to show extensive meandering, in contrast to what was observed in DEIMEC-I. Two surface drifters deployed during the survey further demonstrated that the turbulence principally consisted of series of eddies travelling east (Ansorge and Lutjeharms, 2005).

A sharp SSH gradient, altimetrically identified, was found to correspond closely to an intense front during DEIMEC-III. A detailed hydrographic study of the front revealed that it consisted of both the SAF and the APF (Ansorge *et al.*, 2004). The juxtaposition of these two frontal systems once more highlighted the variable nature of the physical dynamics induced by the ridge and the fracture zone on the ACC. Highest values of total integrated chlorophyll_a (22.8 mg chl-a m^{-2}) were observed to coincide with the location of this double front, while elsewhere, values ranged between 4 and 11 mg chl-a m^{-2}.

The last in the series of the DEIMEC cruises, undertaken in 2005, extensively surveyed an intense (< -40 cm) negative SSH anomaly (Ansorge *et al.*, 2006). As anticipated, the anomaly was found to match the position of a cold eddy. The feature was about 200 km in diameter and more than 1 km deep. Water masses associated with this eddy suggested unambiguously that the feature originated south of the APF. This particularly interesting eddy was studied in great detail (Bernard *et al.*, 2007; Swart *et al.*, 2008). De Szoeke and

Levine (1981) have suggested that mesoscale features in the Southern Ocean could play a crucial role in meridional heat flux required to compensate heat loss through air-sea interactions. With that in mind, the total available heat and salt anomaly associated with the eddy relative to the surrounding was calculated (Ansorge *et al.*, 2006; Swart *et al.*, 2008).

At the culmination of the DEIMEC programme, the main objectives to follow the advection of eddies from their source region, to hydrographically characterise them and to study their biological impact had been reached. The collocation observed after MOES-II and MIOS-II between sea surface height anomalies and marine eddies had unequivocally been established.

Nonetheless, the hostile environment of the Southern Ocean hampers hydrographic expeditions to such extent that these are usually limited to austral summers. A continuous dataset is necessary in order to understand numerous processes associated with the ACC. Unfortunately, in spite of having excellent spatial and temporal coverage, satellite remote sensing is limited to providing information for the upper skin of the sea surface only. Numerical models, on the other hand, provide an efficient representation of the complex ocean dynamics. Moreover, the simulation of oceanic processes provides information even in data-sparse regions.

2.2. Model Studies of the South-West Indian Ridge Region to date.

Ranging from simple mechanistic to complex simulation, models are widely used. Different kinds of numerical models are available, namely, primitive equations models, coastal models, and coupled ocean-atmosphere models.

In order to investigate the dynamic nature of the Southern Ocean, an eddy-resolving model with sufficiently high horizontal resolution is needed. The Fine Resolution Antarctic Model (The FRAM group, 1991) is arguably the first major primitive equation model which allowed many processes associated with the ACC to be studied (e.g. Wells

and de Cuevas, 1995; Best et al., 1999). Of particular importance, the meridional overturning was observed to occur along isopycnal surfaces (Döös and Webb, 1994). The FRAM Atlas (Webb *et al.*, 1991), a collection of temperature, salinity, velocity and pressure snapshots from the FRAM model, was critical in the design of oceanographic cruises in the Southern Ocean as part of the WOCE programme.

Many major model studies of the Southern Ocean and of the ACC have been carried out. Building on the Semtner and Chervin's Global Model (Semtner and Chervin, 1988), Maltrud *et al.* (1998) produced the faster Parallel Ocean Program (POP) model which they have used to test various forcing combinations. Marsh *et al.* (2000) have used the Miami Isopycnal Coordinate Ocean Model (MICOM; Bleck *et al.*, 1997) to investigate the water mass transformation in the Southern Ocean. MICOM uses a vertical coordinate system that favours horizontal mixing along surfaces of constant density. The CSIRO coupled ocean-atmosphere model (Gordon and O'Farrell, 1997) has been used to understand the Southern Ocean response to climatic changes (Hirst, 1999) and more recently, the Ocean Circulation and Climate Advanced Modelling (OCCAM) project (Webb *et al.*, 1998a) has been used to study eddy related transport in the Antarctic (Lee and Coward, 2003).

In the vicinity of the SWIR, two simple free inertial jet model (Niiler and Robinson, 1967) studies have been undertaken. This particular model describes the balance between the curvature of the current, the planetary vorticity (β – latitudinal change in Coriolis effect) and the stretching caused by topography so as to maintain constant transport.

Gouretski and Danilov (1993) have presented results of the first regional simulations of the flow at the SWIR. They initiated five jets between 49.5°S and 51.5°S along 22°E, four of which showed a sharp southward excursion through the ABFZ and meandering east of the ridge. They further noted that the deflection of the jets were in response to bottom velocities varying between 1 – 8 cms^{-1}. More importantly, their results further confirmed that the fracture zone indeed constricted the flow of the ACC causing it to meander and subsequently, advect eddies into the Enderby Basin. Further simulations by Craneguy and

Park (1999) revealed that bottom velocities between 2 and 4 cms^{-1} are sufficient to dissever the SAF and the APF. This is a direct result of the topographic control of the SWIR on the primarily barotropic ACC.

2.3. Summary.

Following the MOES-II and MIOS-II surveys, the complexity of the physical setting of the Prince Edward Islands was established. The increased biological activity previously only observed around the islands was found to be in direct response to the physical dynamics at the South-West Indian Ridge (Froneman *et al.*, 1999; Pakhomov *et al.*, 2000b). The SAF and APF, carrying the core of the ACC, are highly variable east of the ridge (Pakhomov *et al.*, 1998, 2003; Perissinotto *et al.*, 2000; Lutjeharms *et al.*, 2002). On occasion, the SAF splits into a northern and southern branch. Moreover, the southern branch of the SAF tends to merge with the APF at the ridge forming a double front (Pakhomov *et al.*, 2000b; Froneman *et al.*, 2002) and creating a distinct biological barrier (Bernard and Froneman, 2003; Ansorge *et al.*, 2004). Close to the islands, the SAF is deflected north-eastward (Ansorge *et al.*, 1999; Pakhomov *et al.*, 2000b). Further east, in the Enderby Basin, the ACC is highly fragmented (Holliday and Read, 1998; Pollard and Read, 2001) primarily as a result of the loss in topographic control of the APF.

Satellite altimetry provided further insight on the turbulence observed close to the islands. Eddies generated at the SWIR, as a result of the conservation of vorticity as the ACC is channelled through the Andrew Bain Fracture Zone, closely correlate to sea surface height anomalies from altimetry (Ansorge and Lutjeharms, 2003, 2005; Pakhomov *et al.*, 2003; Ansorge *et al.*, 2004, 2006). The DEIMEC programme (Figure 2.2) allowed detailed hydrographic studies of these mesoscale features. Table 1 summarises what transpired from these surveys. Latest results further suggest that the enhanced mesoscale variability associated with the ridge could have profound climatological impact, not only for the islands downstream, but for the global heat and salt budget (Ansorge *et al.*, 2006).

The SWIR region stands out in a relatively quiescent surrounding. The oceanic environment around the Prince Edward Islands sustains the abundant bird life and marine

	Cold Eddies		Warm Eddies	
Sea Surface Height Anomaly	Negative		Positive	
Intense SSHA	< -30 cm	(B)	> +25 cm	(A)
	< -40 cm	(D)	> +40 cm	(B)
Number of Intense SSHA/year	3	(D)		
Rotation	Clockwise		Anti-Clockwise	
Diameter	125 km	(B)	250 km	(B)
	175 – 200 km	(D, E)		
Depth	> 1000 m	(D)	> 800 m	(B)
Geostrophic speed (boundary)	0.69 ms^{-1}	(B)	0.35 – 0.5 ms^{-1}	(B)
	0.45 – 1.40 ms^{-1}	(D)		
Geostrophic speed (core)	0.08 – 0.10 ms^{-1}	(D)	0.08 – 0.10 ms^{-1}	(B)
Surface Water	AASW		SASW	
	< 4°C, < 33.70	(C)	> 5°C, > 33.85	(C)
	4.2 – 4.4°C,	(D)		
	33.77 – 33.83	(D)		
Sub-Surface Water	WW		Salinity Maximum	
	< 0.4°C, 34.1	(D)	4.09°C, 34.1	(B)
Advection speed	2 – 5 km/day	(A)	2 – 5 km/day	(A)
	4 – 8 km/day	(B)		
	2 km/day	(D)		
Longevity	7 – 11 months	(D, E)	9 – 11 months	(A)
Available Heat Anomaly	-5.3×10^{19} J	(E)		
Available Salt Anomaly	-6.34×10^{11} kg	(E)		

Table 1: Hydrographic characteristics of cold and warm eddy based on CTD, XBT, drifter and float data following MOES-II, MIOS-II, DEIMEC cruises. (A) – Ansorge and Lutjeharms, (2003); (B) – Ansorge and Lutjeharms, (2005); (C) – Pakhomov *et al.*, (2003); (D) – Ansorge *et al.*, (2006); (E) – Swart *et al.*, (2008).

mammals found on the islands. Grey-headed albatrosses from the islands have been tracked and there is evidence that these birds feed on the edges of eddies generated at the ridge (Nel *et al.*, 2001). On-going research, seeking to understand the behaviour of mammals on the islands, has shown that seals adopt a similar trajectory in their foraging preference (Jonker and Bester, 1998). The ecological dependence on these transient mesoscale features may therefore be profound.

In response to an average warming of the Southern Ocean by 0.17°C observed by Gille (2002) since the 1950s, Weimerskirch *et al.* (2003) have postulated a system shift from observations on the behaviour of sub-antarctic top predators. It is likely that this suggested latitudinal shift in the Southern Ocean regime could have an impact on the structure and intensity of the ACC frontal systems and could affect, adversely or otherwise, the distribution of zooplankton usually associated with these fronts (Pakhomov and McQuaid, 1996). A recent study has revealed that over the last 50 years, sea surface temperature at Marion Island has risen by 1.4°C (Mélice *et al.*, 2003). Rouault et al. (2005) have attributed the observed warming to a change in mid-latitude climate and the semi-annual oscillation. The sensitivity of eddy generation in response to this increase in sea surface temperatures remains to be investigated.

Mathematical formulation of the ocean dynamics have helped to successfully elucidate many questions about important processes in the world's ocean. For example, the FRAM model was used to investigate the variability of the south ACC front close to South Georgia (Thorpe *et al.*, 2002; Ward *et al.*, 2002). In all likelihood, using numerical models to investigate the conglomerate nature of the flow of the ACC in the vicinity of the SWIR could be fruitful.

3. RESEARCH QUESTIONS.

The fact that the physical environment of the Prince Edward Islands is extremely variable and productive, has been subject of much interest (Ansorge and Lutjeharms, 2000; McQuaid and Froneman, 2004). Despite the enormous research efforts undertaken over the last two decades, some important questions remain unaddressed.

The variability in the South-West Indian Ridge region is primarily characterized by mesoscale features, eddies, whose geneses result from the ACC's interaction with the ridge. The edges of these features may retain nutrients and have been shown to be a preferential foraging ground for birds and mammals living on the archipelago (Jonker and Bester, 1998; Nel *et al.*, 2001). The underlying mechanism favouring the possible retention of nutrients round the edges of eddies has been inferred (Nel *et al.*, 2001) and remains inconclusive. The plankton community structure is very dependent on nutrient exchanges that are associated with these fugacious features suggesting that the turbulence at the ridge has far reaching ecological implications. It is therefore necessary to understand the exact nature of the chemistry and the subsequent impact on plankton communities and higher trophic predators.

The marine ecosystem of the region appears to depend strongly on the meridional exchanges of water masses by eddies. The high temporal variability in the position of the SAF and APF suggest that exchanges in water masses may also vary in time. In addition, the SAF and APF have been observed to merge at times forming a distinguishable biological boundary (Bernard and Froneman, 2003). The precise effect of such merging of these two hydrological barriers on eddy generation and trajectory is yet to be investigated.

The two primary components responsible for the unstable and seemingly unpredictable flow at the South-West Indian Ridge are the ACC and the ridge itself. Resolving the precise role of the ridge in causing the turbulence could be one step closer towards possibly predicting the frequency and strength of mesoscale features shed in that region.

That would entail presetting the other key components and varying the nature of the ridge to study its influence. Similarly, how does varying the ACC flux immediately upstream the Andrew Bain Fracture Zone affect eddy genesis? These open questions are more of academic interest than having direct impact on the ecology of the subantarctic islands downstream.

It is agreed that the Southern Ocean is very vulnerable to climatic changes that have been observed globally (Gille, 2002). The proposed system shift of Weimerskirch *et al.* (2003) suggests that the latitudinal mean position and structure of frontal systems associated with the ACC could change. In addition to the SWIR, the APF within the ACC is another key component responsible for the variability at the ridge. It remains uncertain how sensitive the process of eddy generation would be at the ridge in response to these possible changes in climatic conditions.

Despite the increasing number of hydrographic sections and ARGO profiles available in that region, these questions still can not be address entirely. The need to model the SWIR region has become necessary and is the next logical step in understanding the observed and well documented dynamics. The Ocean Circulation and Climate Advanced Modelling (OCCAM) project was initiated in the early 1990s. Building on the previous successful Fine Resolution Antarctic Model (The FRAM group, 1991), the primary aim of the project, was to study the global ocean circulation in an attempt to further our understanding of the ocean climate and its prediction. The model outputs have been widely and successfully used in Southern Ocean related studies (e.g. Lee *et al.*, 2002, 2007; Pollard and Read 2001; Drijfhout *et al.*, 2003; Lee and Coward, 2003).

3.1. Aims of the Study – Key Questions.

This study proposes to use model outputs from OCCAM to study the circulation at the South-West Indian Ridge. The availability of a comprehensive long-term dataset with high vertical (66-levels) and horizontal (up to $^{1}/_{12}^{th}$ of a degree) resolutions and the readily available support makes the OCCAM outputs ideal for an exploratory study of the

dynamics of the SWIR region. Section 1 of chapter 4 elaborates on the model's configuration.

Prior to using any numerical model, it is vital to ensure that the model correctly represents the status-quo. This is particularly important for a localised study, such as the SWIR region, where the flow of the ACC is so variable. This study focuses mainly on assessing OCCAM's representation of the dynamics at the SWIR. In order to keep the task manageable, the strengths and weaknesses of the model are addressed in three parts.

1. **How well does OCCAM depict the general circulation of the SWIR region?**

   The circulation of the SWIR region is assessed in chapter 5 by looking at mean fields of sea surface temperature, near-surface velocity and eddy kinetic energy. The average locations of the major frontal systems are also evaluated. In addition, the larger-scale dynamics under the influence of the ridge are investigated.

2. **Does OCCAM adequately represent mesoscale features generated at the ridge?**

   The notable characteristic of the SWIR region is the fact that disturbances to the mean flow occur at the ridge and propagate eastwards. The nature of the turbulence is mainly characterised by meanders and eddies. In order to address this question (in chapter 6), it is vital to distinguish between deformation and rotation when locating and tracking mesoscale features. This study adopts a method (described in section 4.5.2) proposed by Isern-Fontanet *et al.* (2003) to help correctly identify and follow eddies. The focus here is set on intense ($|SLA| > 30$ cm), well-defined and persistent (longevity of at least 2-3 months) features.

3. **How do eddies at the SWIR change with age?**

   A serious limitation of using direct hydrographic measurements is the inability of continuous monitoring. Autonomous floats deployed within eddies often spin out and

at times even fail to capture data of acceptable quality. In the literature, information about the decay of anomalies has been inferred from altimetric observations, where the anomalous sea surface height signature of eddies gradually decreases. Eddies have been shown to reach depths of at least 1000 m and there are indications that they may reach even deeper. Using a model, such as OCCAM, to study eddies at the SWIR provides a unique opportunity to examine their decay and water mass transformation. How are the physical characteristics of intense eddies changing downstream of the ridge? This question is particularly important in understanding the biological implications of mesoscale features in that region. High levels of chlorophyll_a have been observed at the edges of cold eddies suggesting an abundant concentration of zooplankton entrained by these features (Bernard *et al.*, 2007; Ansorge *et al.*, submitted). This enhanced biological activity in turn provides a foraging ground for top predators from the Prince Edward Islands. The decay of eddies tracked in chapter 6 are studied further in chapter 7.

For the purpose of the study, the SWIR region is defined by the area bounded by 10°E – 50°E and 44°S – 58°S (Figure 4.4, pg 30). The area chosen is clear of the highly variable Agulhas regime south of Africa (Figure 2.1, pg 7) to avoid contamination from features originating from the Agulhas Current, Agulhas Return Current and the Subtropical Convergence.

4. DATA AND METHODS.

A wealth of data, ranging from in-situ measurements to remotely sensed data, is nowadays available to assist the study of the world's oceans. The oceanographic community is not restricted to using historical hydrographic data which, aside from being sparse, on many occasions made use of inaccurate equipment leading to inhomogeneous datasets. This study draws data from various independent datasets.

4.1. The OCCAM Model.

Most high resolution ocean models are based on the pioneering work of Bryan, Cox and Semtner (Bryan, 1969; Semtner, 1974; Cox, 1984) and OCCAM is no exception. In any ocean numerical model, crucial assumptions are made. These are embedded in the primitive equations derived by Bryan (1969).

$$\frac{\partial u}{\partial t} + (u \bullet \nabla)u + w\frac{\partial u}{\partial z} + f \times u = -\frac{\nabla p}{\rho_0} + D_u + F_u \qquad (1)$$

$$\frac{\partial S}{\partial t} + (u \bullet \nabla)S + w\frac{\partial S}{\partial z} = D_S + F_S \qquad (2)$$

$$\frac{\partial T}{\partial t} + (u \bullet \nabla)T + w\frac{\partial T}{\partial z} = D_T + F_T \qquad (3)$$

$$\rho g = -\frac{\partial p}{\partial z} \qquad (4)$$

$$\nabla \bullet u + \frac{\partial w}{\partial z} = 0 \qquad (5)$$

$$\rho = \rho(T, S, p) \qquad (6)$$

f – Coriolis term: $f = 2\Omega\sin(\theta)$ Ω – rotation rate of the earth
θ – latitude

u – Horizontal velocity.
S – Salinity.
p – Pressure.
D – Diffusion term.
w – Vertical velocity.
T – Potential Temperature.
ρ – Density.
F – Forcing term.

The horizontal momentum equation (1) incorporates the assumption that small changes to density are neglected, unless the effect is on the horizontal pressure gradient. The hydrostatic equation (4) assumes that the vertical velocities, being small, can be ignored. The continuity equation (5) takes into account the assumption that the ocean is incompressible. Equation (2) and (3) describe the three dimensional advection and diffusion while equation (6) is the equation of state.

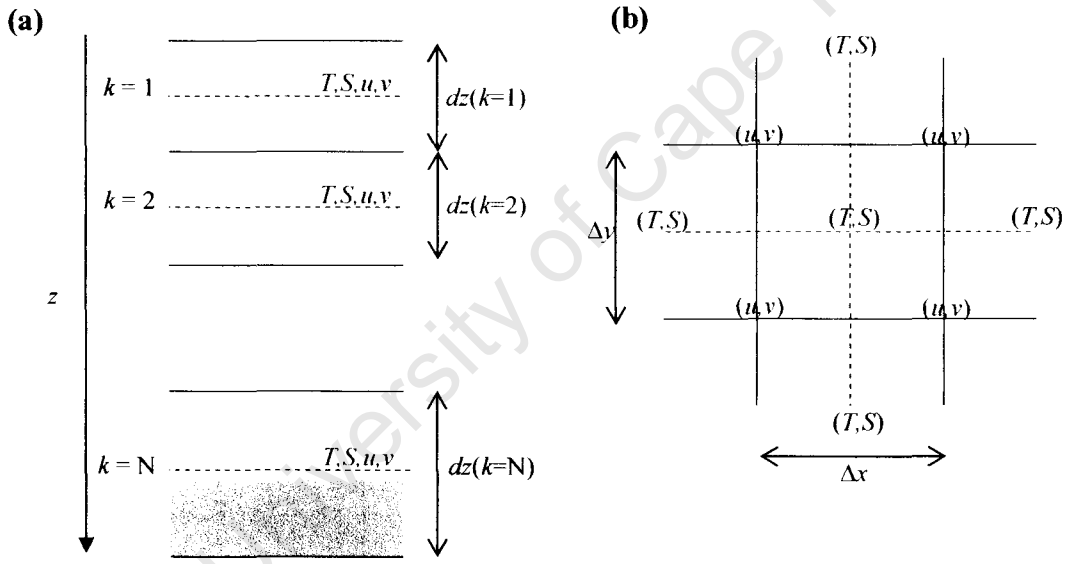

Figure 4.1: Vertical and horizontal arrangement of variables. (a) In the vertical plane, tracers and horizontal velocities are defined at the centre of the box (Adapted from Cox, 1984). *dz* represents the thickness of the *k*'th box and level k = N represents the bottom box which is partially filled (see text). (b) The arrangement of variables in the horizontal plane follows the Arakawa-B grid (Adapted from Bryan, 1969). Δx and Δy are the horizontal resolution in longitude and latitude respectively. The velocity grid is offset from the tracer grid by $\frac{1}{2}\Delta x$ and $\frac{1}{2}\Delta y$.

The equations (1) – (6) are solved in discrete, equal time-steps. Time-stepping is achieved using the leapfrog (mid-point rule or step-over) scheme, the Euler scheme and the Matsuno (Euler-backward) predictor-corrector scheme. The latter is used as a correction to prevent splitting of the solution on even and odd time-steps (Webb *et al.*, 1998a). A description of these time differencing schemes is given by Mesinger and Arakawa (1976).

The barotropic and baroclinic part of the ocean are calculated separately and Table 2 gives the time-steps used for the 1°, $^1/_4$° and $^1/_{12}$° horizontal resolution.

	1 °	$^1/_4$ °	$^1/_{12}$ °
Time-step for tracers and baroclinic velocities	3600	900	300
Time-step for barotropic velocities	72	18	6

Table 2: Time-step (in seconds) used for the barotropic and baroclinic parts of the calculations at different resolution.

The OCCAM model uses a scaled coordinate in the vertical (Marti *et al.*, 1992). In this scaled coordinate, the level spacing is equal. Variables are defined in the middle of the k'th box (Figure 4.1a). The relationship between depth z and level k is given by

$z(k)$ = depth of the bottom of the k'th layer

$$= (a \times k) + \left(b \times d \times \log \left(\frac{\cosh\left((k-c)/d \right)}{\cosh\left(-c/d \right)} \right) \right)$$

$a = 10725.0$

$b = 10275.0$

$c = 36.0$

$d = 13.0$

(Values of the constants are for the OCCAM 66-Levels runs).

The arrangement of variables in the horizontal follows the so-called Arakawa-B grid (Arakawa, 1966). The velocity grid is offset from the tracer grid by half the horizontal resolution (Figure 4.1b). The advantages of using this grid method are outlined in Webb *et al.* (1998a) – better representation of ocean fronts and simpler velocity boundary conditions.

OCCAM – Original Version.

The original OCCAM code was adapted from the Modular Ocean Model (MOM) (Pacanowski *et al.*, 1990) and designed to run efficiently on an array of processors

(Webb, 1996). Three important improvements were made, details of which are thoroughly described in Webb *et al.* (1998a). First, the rigid-lid was replaced with a free surface scheme that used a tidal model to resolve the barotropic equations. Secondly, following a method developed by Webb *et al.* (1998b), the advection scheme was improved. Finally, the OCCAM model introduced two model grids in the horizontal to avoid singularity at the North Pole.

Replacing Bryan's (1969) rigid-lid approximation requires considering the effect of high frequency surface gravity waves. The main benefit of the rigid-lid approximation was that the time-step used in the Bryan's model was increased by an order of magnitude, which had a direct desirable impact on solving the equations. The scheme adopted in OCCAM follows that described by Killworth *et al.* (1991) with some added features to increase its efficiency. A simple tidal model is used to resolve the barotropic equations.

Figure 4.2: The OCCAM model grids. Model 1 covers the Indian, Pacific, South Atlantic and Southern Oceans while Model 2 covers the North Atlantic and Artic Oceans. Model 2 is rotated orthogonally and meets Model 1 at the Equator in the Atlantic (Coward *et al.*, 1994).

The Quadratic Upstream Interpolated for Convective Kinematics (QUICK) advection scheme by Leonard (1979) was improved by Webb *et al.*, (1998b) resulting in the Modified Split-QUICK (MSQ) scheme. This scheme can be used to simulate advection of

tracers both in the horizontal and in the vertical. The Split-QUICK (SQ) scheme effectively splits the QUICK operator into two terms – the first term being the fourth order advection operator and the second term, the velocity dependent biharmonic diffusion operator. There is no loss in efficiency in the SQ scheme. In the MSQ, increased accuracy is achieved by modifying the advection operator.

In the horizontal, a unique setup is adopted in OCCAM where two model grids are defined (Coward *et al.*, 1994). Model 1 is used for the Indian, Pacific, South Atlantic and Southern Oceans and Model 2 covers the North Atlantic and the Arctic Oceans (Figure 4.2). The main reason for this peculiar setup is to avoid convergence of the longitudes in the Arctic Ocean. Otherwise, a very small time-step would be needed to adequately resolve the equations and this would be computationally very expensive. The boundaries between Model 1 and 2 are defined at the Equator in the Atlantic and in the Bering Strait, where a simple channel model is used to link the two models.

OCCAM – Final Version.

The original version of the OCCAM model had 36 levels in the vertical and a horizontal resolution of ¼ of a degree. In the late 1990s, major changes were made and the physics of the model was improved. A new generation of the OCCAM global ocean model was then developed. The setup of this version is documented by Coward and de Cuevas (2005). A summary of the model setup is described next.

The vertical resolution was increased to 66 levels. The motivating factor for this increase was to achieve better representation of the mixed-layer dynamics. With 14 levels in the upper 100 m, the euphotic zone can be modelled not only physically, but also biogeochemically. To that end, a hierarchy of OCCAM runs with various horizontal resolutions was introduced and the OCCAM 1^{o} model was extended to incorporate the biogeochemical oxygen and carbon cycle. Sinha and Yool (2006) have provided a complete technical discussion of this major coupling task. In addition to the increased resolution in the vertical, the improved OCCAM model was made more realistic in many aspects.

The Pacanowski and Philander (1981) vertical mixing scheme was replaced by the K-Profile Parameterisation (KPP) proposed by Large *et al.* (1994). The KPP scheme is an oceanic boundary layer model which effectively simulates the exchanges between the boundary layer and the thermocline. Moreover, given correct surface forcing and advection, the KPP scheme ensures satisfactory results irrespective of the vertical resolution and coordinate system used.

Isopycnal mixing was introduced in an attempt to represent changes to water properties better in the non eddy-resolving version of OCCAM. A discretisation method by Gent and McWilliam (1990) was used to calculate the isopycnal diffusive flux for tracers in the $^1/_4^\circ$ eddy-permitting simulation. The $^1/_{12}^\circ$ on the other hand is eddy-resolving and therefore should not require the implementation of an isopycnal mixing scheme.

The topography used in OCCAM 66-levels is derived from a number of products namely the Sandwell and Smith (1995) topography, the International Bathymetric Chart of the Arctic Ocean (IBCAO; Jakobsson *et al.*, 2000) and the US Digital Bathymetric Data Base 12 minute data (DBDB5, 1983). OCCAM uses partial bottom cells (Pacanowski and Gnanadesikan, 1998) in order to better match the bottom topography. In the bottom box, tracers are still defined at the centre of the box (Figure 4.1a).

A sea-ice model has been coupled with OCCAM providing accurate and detailed simulation of sea ice evolution and ocean circulation (Aksenov, 2002). The model consists of two distinct parts. Based on Semtner's (1976) thermodynamics, the model's thermodynamical part caters for the sea-ice thermal evolution. The dynamical part of the model consists of components such as the momentum balance, the elastic-viscous-plastic ice rheology and the ice advection and adjustments. The combination of these two crucial parts makes the ocean-ice coupled model versatile to various frameworks and convenient, lending itself to experiments of academic interest.

The model tracer fields were initialised using the WOCE SAC climatology, the World Ocean Atlas and the Arctic Ocean Atlas data and the velocity fields set to zero (Coward

and de Cuevas, (2005). Surface forcing in the OCCAM 66-levels is achieved using a bulk layer formulation for heat and momentum. This eliminates the need for surface potential temperature relaxation. Atmospheric fields such as the 10 m wind speed; the 2 m air temperature and specific humidity; cloud fraction, solar radiation and precipitation, have been combined with the top level potential temperature to calculate the wind stress, the turbulent fluxes and the net long wave radiation. The 6-hourly wind speed, air temperature and specific humidity were obtained from NCEP reanalysis (Kalnay *et al.*, 1996). Monthly precipitation is a combination of satellite microwave data and observations (Spencer, 1993; Xie and Arkin, 1996), while cloud fraction and solar radiation data are from the ISCCP dataset (Rossow and Schiffer, 1991).

Properly representing the precipitation and evaporation is of essence because of their effects on the height of the free surface and the salinity of the top layers. The fresh water flux is calculated using the precipitation field and evaporation (calculated from the air-sea transfer equations). Salinity relaxation towards the monthly Levitus *et al.* (1998) is still used over the upper 20 m with a 45 days time scale. This is an attempt to ensure that the lack of explicit runoff and any deficiencies in the precipitation fields are accounted for.

Model Outputs.

Various runs of the OCCAM 66-level global ocean model have been made. The OCCAM 1° model is widely used for testing purposes before implementing any schemes. Moreover, many experiments have been carried out at that resolution (e.g. the biogeochemical model coupling). The present study uses Run 103 ($^{1}/_{4}^{\circ}$ horizontal resolution) and 401 ($^{1}/_{12}^{\circ}$ horizontal resolution) between the years 1989 – 1998 (inclusive). Both runs have no initial spin-up since a $^{1}/_{12}^{\circ}$ spin-up would be computationally very expensive. The advantage of this approach is that both runs would lend themselves to direct comparison (de Cuevas, *personal communication*). The runs start from year 1985 to year 2004. Run 401, however, only reached year 1999 at the time data were extracted.

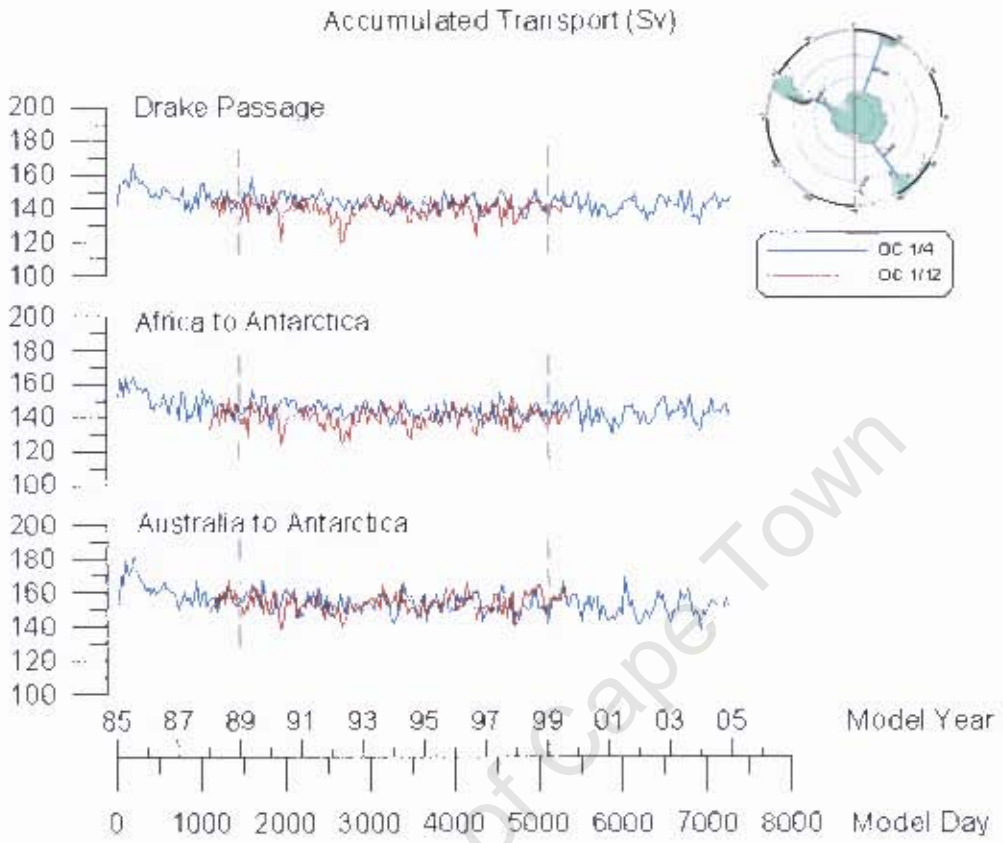

Figure 4.3: Full-depth (66 levels) accumulated monthly averaged transport in Sv (1 Sv = 10^6 m^3s^{-1}) at the Drake Passage, between Africa and Antarctica and between Australia and Antarctica. The dashed lines indicate the 10-year period between 31 Dec 1988 (model day 1460) and 29 Dec 1998 (model day 5110) of data used for this study. Both runs of the model are stable from 1989 onwards.

Figure 4.3 shows the accumulated monthly averaged transport for the ACC at the Drake Passage, south of Africa and south of Australia for Run 103 (OC-4) and 401 (OC-12). It is immediately evident that from 1989 onwards, the ACC transport reaches equilibrium with an average of ~140 Sv at the Drake Passage, ~145 Sv between Africa and Antarctica and ~155 Sv between Australia and Antarctica. An apparent eastward increase in transport as well as some degree of annual and inter-annual variability is observed. These values reasonably fall within the range of calculated full-depth estimates of ACC transport in previous work (e.g. Whitworth and Peterson, 1985; Cunningham *et al.*, 2003; Park *et al.*, 2001; Rintoul and Sokolov, 2001; Legeais *et al.*, 2005). North Atlantic Deep Water (NADW) being added in the South Atlantic accounts for the additional transport east of the Drake Passage leading to an increase in salinity signature of the Circumpolar

Deep Water (CDW) in the south-west Indian Ocean sector of the Southern Ocean as observed by Read and Pollard (1993). South of Australia, Yeremchuck *et al.* (2001) estimated the ACC transport to be 151 ± 50 Sv.

Coward and de Cuevas (2005) have given a detailed description of all the variables available from the model. In the present study the following primary model variables are used:

3-D Fields	*2-D Fields*
Potential Temperature.	Sea Surface Height.
Salinity.	Sea Level Pressure.
U component of horizontal velocity.	
V component of horizontal velocity.	
(The velocity fields are total barotropic and baroclinic velocity).	

The 10-year (31 Dec 1988 – 29 Dec 1998) 5-day-mean data were extracted in MATLAB .MAT data format. The $^1/_4^o$ (OC-4) run of the model is eddy permitting while the $^1/_{12}^o$ (OC-12) is eddy resolving, with a grid size of ~9.3 x ~5.8 km over the SWIR domain. The SWIR region being characterised by high levels of mesoscale turbulence, the $^1/_{12}^o$ run is favoured over the $^1/_4^o$. Both runs are used for the initial model validation of the SWIR region. The finer resolution is further used for a detailed investigation of the model's representation of turbulence at the ridge.

4.2. Hydrographic Sections.

Although over the last decade, many cruise expeditions were made to the Prince Edward Islands and around the South-West Indian Ridge region, only two major cruise sections are used in this study. The OCCAM model output used in this study is only available for the years 1989 to 1998 (inclusive). Therefore, for consistency in comparison the choice of hydrographic data used is restricted to sections occupied between 1989 and 1998.

CIVA.

The WOCE (World Ocean Circulation Experiment) Hydrographic Profile section I06 along 30°E has been occupied twice by two cruises namely CIVA-1 and CIVA-2 on board the French vessel, the RV Marion Dufresne (Park and Charriaud, 1997; Park *et al.*, 1993, 2001). The CIVA-1 cruise was undertaken from January – March 1993 from 69°S to 44°S with 52 full-depth CTD stations. The CIVA-2 cruise, March 1996, was a repeat of the CIVA-1 cruise and completing the gap between 44°S and Africa with a total of 94 full-depth CTD stations. Neil-Brown CTDs were used in both cruises with station intervals of 20 nautical miles near frontal regions extending to 40 nautical miles south of 53°S.

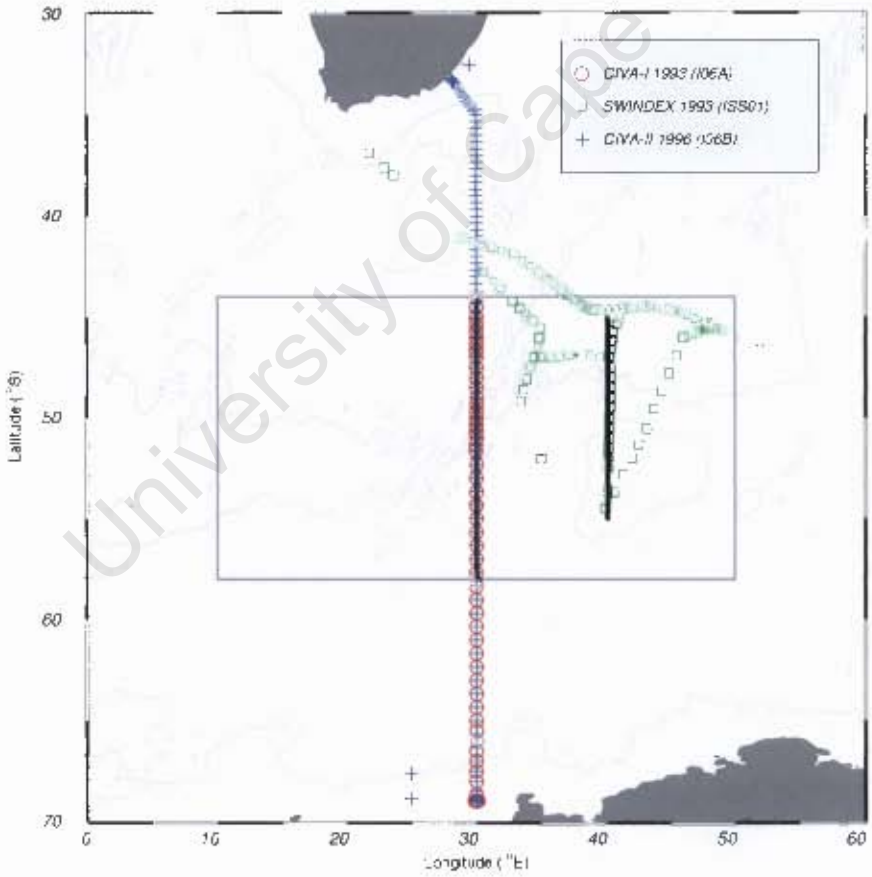

Figure 4.4: Cruise tracks showing station locations for CIVA-1 (WOCE I06A), CIVA-2 (WOCE I06B) and SWINDEX (WOCE ISS01). Sections used in this study are shown with two black lines along 30°E and 40°E, between 44°S and 58°S for CIVA-1 & 2 and between 45°S and 55°S for SWINDEX respectively. The SWIR region of interest is shown with the grey rectangle (44°S – 58°S; 10°E – 50°E). The 4000 m isobath is shown.

SWINDEX.

The South-West Indian Ocean Experiment (SWINDEX) was undertaken in March – May 1993 on board of the RV Discovery (Voyage 201). This WOCE ISS01 expedition consisted of four sections, three of which were made across the Antarctic Polar Front between 28°E and 50°E. The expedition, with a total of 97 full-depth CTD stations, served to observe the structure of the ACC and the path taken by the current when encountering the Crozet Plateau (Pollard *et al.*, 1994).

The CIVA and SWINDEX datasets were downloaded from the WOCE Hydrographic Program Office (WHPO) online data centre. Figure 4.4 shows the tracks and stations for the three cruises and sections used in this study.

4.3. Drifters.

The WOCE Surface Velocity Program (now Global Drifter Program) has, since 1990, seeded the world's ocean with numerous surface drifters. The aims of the program are to map the global currents and temperature in the surface mixed layer, to improve parameterisation and verify models and to obtain the distribution of horizontal kinetic energy (WOCE-SVP report No.1, 1988). The data used for this study was acquired from the Data Assembly Centre (DAC) at the Atlantic Oceanographic and Meteorological Laboratory (AOML). The DAC is responsible to diligently apply uniform quality control, edit and interpolate data into 6-hour intervals using the kriging method. The WOCE-GDP laid out strict standards to ensure acquisition of reliable and homogeneous data. Furthermore, drifters were drogued at a depth of 15 m, designed to increase the drag area ratio, in order to reduce to a strict minimum the value of the erroneous velocity component due to the direct wind action.

The dataset used in this study consists of all drifter velocity data available for the region bounded by 44°S – 58°S and 10°E – 50°E between January 1987 and June 2005.

4.4. Satellite Remote Sensing Data.

Having the advantage of looking at a vast area in a relatively short time, remotely sensed ocean parameters offer a quasi-synoptic view of the sea surface. This is ideal for studying both the short and long term variability of the oceans. For the purpose of this study, two remote sensing products were used, namely, satellite altimetry and sea surface temperature.

Altimetry.

Satellite altimetry uses active sensors, emitting pulses and measuring the time taken for the reflection to reach the sensor. Two main types of altimetry products are available, near-real time (NRT) and delayed time (DT). Furthermore, data can be obtained either from a single satellite or merged multi-altimeter missions. Merged data significantly reduces error in mapping (Le Traon *et al.*, 1998) and DT products are more precise than NRT products (SSALTO/DUACS, 2006). Merged products have been shown to give more realistic estimates of sea surface height, geostrophic velocity and energy than single-mission products (Ducet *et al.*, 2000).

Delayed-time merged products from two satellites, Topex/Poseidon and ERS-1/2 or Jason-1 and Envisat, were used in this study. Data from each mission are homogenised and quality controlled separately, with tidal and inverse barometer corrections applied. Prior to merging, a cross-calibration process ensures that long wavelength errors and any biases are accounted for. Finally, the merged products are quality controlled before being available for download (SSALTO/DUACS, 2006).

The horizontal resolution of the gridded data is $^1/_3$ of a degree on a Mercator grid which is on average 23.2 km over the SWIR domain. Seven-day mean Sea Level Anomaly (SLA) and sea surface geostrophic current data for the period between 14 Oct 1992 and 18 Jan 2006 were acquired via ftp.

AMSR-E.

Sea surface temperature (SST) remotely sensed from space is passive. The Japanese Advance Microwave Scanning Radiometer (AMSR-E) launched on board of the NASA Aqua satellite in 2002 measures important geophysical parameters such as SST and sea surface winds. Complete and continuous measurement is achieved by the ability of the sensor to see through clouds. Missing SST values are generally attributed to sun glint, high wind speed ($> 20\ ms^{-1}$) and near sea ice.

The AMSR-E dataset used for this study consists of weekly SST products downloaded via ftp for the period between 01 Jun 2002 and 23 Sep 2006. Horizontal resolution of the gridded data is 0.25^{o} x 0.25^{o}. The Tropical Rainfall Measuring Mission (TRMM) Microwave Imager (TMI) provides a longer dataset of uninterrupted SST measurements. However, TMI's equatorial orbit limits observations to latitudes between 40^{o}N and 40^{o}S.

4.5. Data Manipulation and Methods.

The datasets used for this study were obtained from different sources (details of which can be found in the Acknowledgement section). The processing required prior analysis was dependent on the format of the data acquired. Hydrographic and drifter data were available in ASCII format, satellite data (altimetry and AMSR-E) were downloaded in NetCDF and output from the OCCAM model were extracted in MATLAB .MAT data-files.

The Ocean Data View (ODV) software, freely available online, offers an interactive environment in which gridded data can be imported and geographically plotted with ease (Schlitzer, 2007). ODV is designed to enable straight forward import of WOCE-WHP data. Moreover, ASCII data in spreadsheet format can also be read and imported. For this reason, ODV was chosen to plot the CIVA and SWINDEX hydrographic sections as well as drifter data. Owing to ODV's high level of abstraction, the software offers limited flexibility.

MATLAB is a high-level, general purpose, scientific programming language that provides an environment for data manipulations and graphical representations. With its ability to perform calculations with maximal numerical precision and its versatility, MATLAB has now proven itself to be very popular amongst the scientific and engineering community. Simple scripts and functions can be written to perform routine procedures on matrix data. Advance algorithms are available enabling data analysis and visualisation of outputs. M_map is a set of mapping tools for MATLAB which is freely available online (Pawlowicz, 2006). Having a coastline and bathymetry resolution of $^1/_4{}^o$ and 1^o respectively, m_map libraries were used to produce final plots after analysis. Remote sensing products were available in NetCDF (Network Common Data Form) format. This acclaimed method to store and share scientific data requires an interface for data access. The necessary interface was downloaded. MATLAB scripts and functions (M-files) were formulated to process all the data.

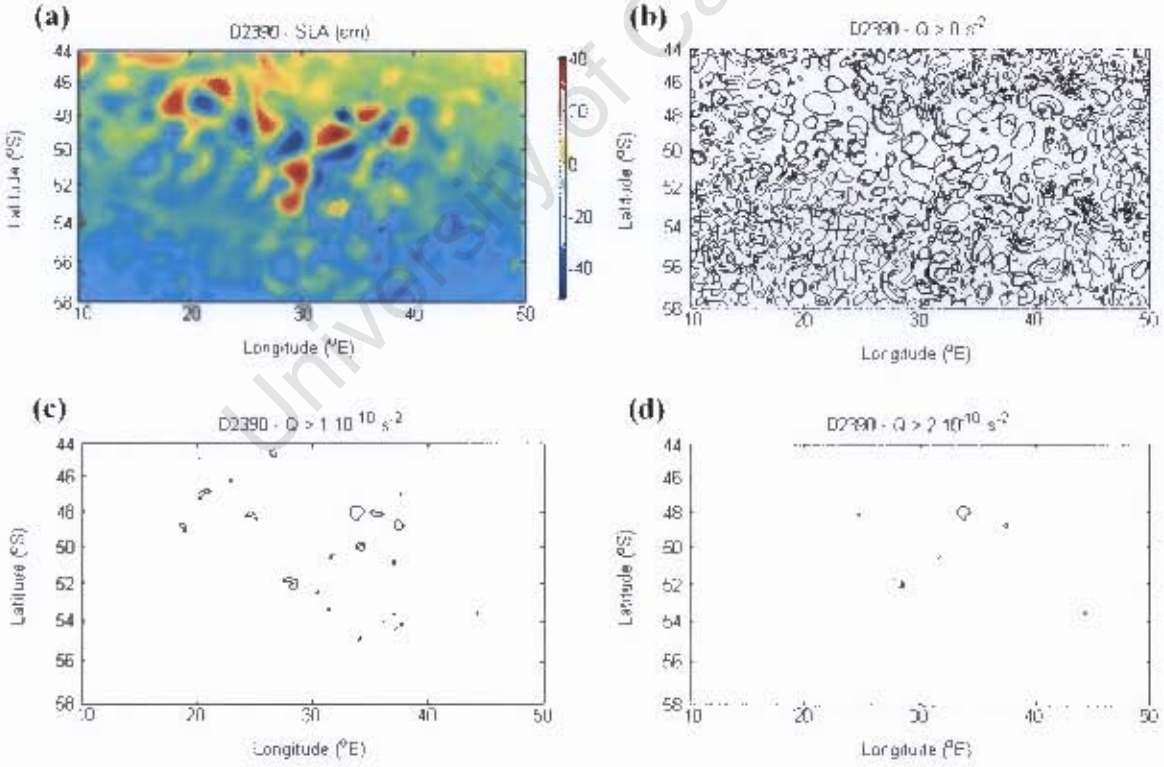

Figure 4.5: (a) Sea Level Anomaly field for D2390 (cm). The Q field was calculated from the horizontal velocities and possible thresholds (b) $Q > 0\ s^{-2}$, (c) $Q > 1 \times 10^{-10}\ s^{-2}$ and (d) $Q > 2 \times 10^{-10}\ s^{-2}$ applied. The second threshold appears to be the most appropriate, when compared to the SLA field.

4.5.1. General Circulation at the Ridge.

The repeat CIVA lines and the SWINDEX line were used as a reference to investigate the general position and structure of the frontal bands associated with the ACC in the SWIR region. Sections of potential temperature and salinity were drawn for the upper 930 m for both datasets. The drifter velocity dataset was used in an attempt to compare OCCAM's (OC-4 and OC-12) representation of the near-surface circulation in the SWIR region. The drifter dataset was initially processed to remove data from undrogued drifters before being spatially averaged over 1^{o} x 1^{o} grids. Surface temperature and kinetic energy were derived from the AMSR-E and altimetry respectively.

4.5.2. Identification and Tracking of Eddies.

OCCAM Sea Surface Height from 5-day-mean fields were averaged over the ten years period (*meanSSH*) and the individual Sea Level Anomaly (SLA_t) fields were calculated. The inverse barometer effect, stating that sea level rises by ~1 cm per 1 millibar decrease in pressure, was taken into account to give

$$SLA_t\,(cm) = SSH_t - meanSSH - 0.995(meanSLP - SLP_t).$$

where $meanSLP = 1010.98$ mb; SSH_t = Sea Surface Height at time t and SLP_t = Sea Level Pressure at time t.

Two potential methods of identifying mesoscale oceanic eddies were explored. Firstly, Gairola *et al.* (2001) have detected eddy signatures from altimetry using dynamic topography. They used a matched-filtering method after applying all possible correction to the raw data. Their technique was found to be suitable for locating eddy signatures along satellite tracks. Secondly, Isern-Fontanet *et al.* (2003), adopting a general method developed by Jeong and Hussain (1995), have derived a Q parameter representing the balance between shear strain rate and vorticity from a two-dimensional velocity field where

$$Q = -\left(\frac{\partial u}{\partial x}\right)^2 - \left(\frac{\partial v}{\partial x}\right)\left(\frac{\partial u}{\partial y}\right)$$

(u, v) – Horizontal Velocity.

Eddies are identified by clusters of positive Q values, where in an elliptic fluid flow, rotation dominates deformation. Choosing an adequate threshold for Q is necessary in order to capture connected entities. However, the choice of a threshold is subjective.

The second method was found to be more appropriate to locate eddies within OCCAM. Using the model horizontal velocities, the Q-fields were calculated for every 5-day-mean. The SLA field (Figure 4.5a) for model day 2390 (19 Jul 1991) is used as an example to illustrate the choice of an adequate threshold. Figures 4.5b-d show regions identified when potential thresholds are applied to the Q-field. Evidently, simply using $Q > 0\ s^{-2}$ is much too lenient, capturing all regions where rotation dominates deformation. So as to limit selection and only identify eddy cores, a higher threshold is necessary. Choosing $Q > 2 \times 10^{-10}\ s^{-2}$ is much too stringent while $Q > 1 \times 10^{-10}\ s^{-2}$ appears to be more appropriate when compared to the SLA.

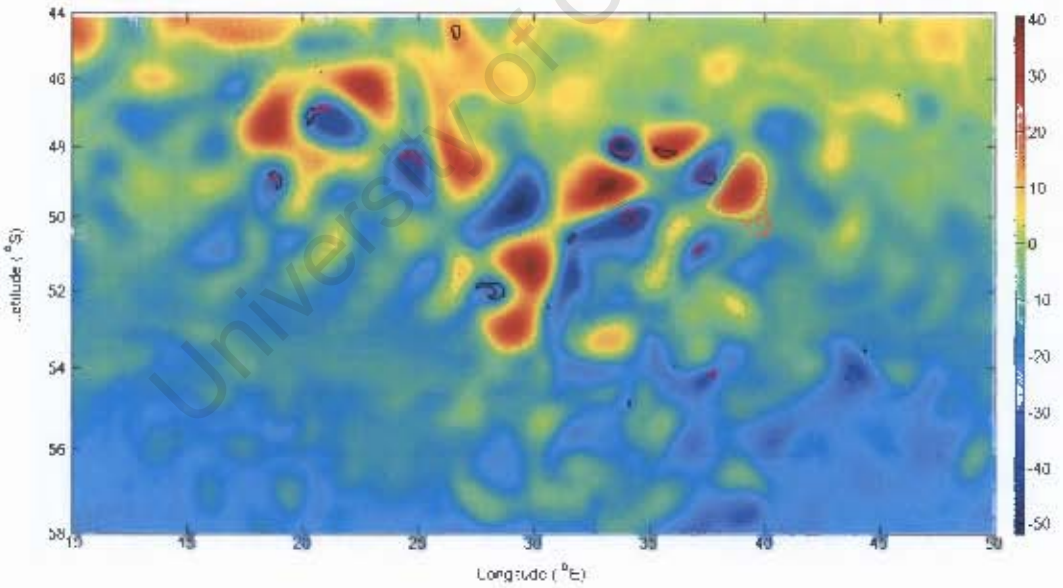

Figure 4.6: SLA field (cm) for D2390 overlaid by the selection fields. In black, $Q > 1 \times 10^{-10}$ s^{-2} and SLA > + 15 cm or SLA < - 15 cm. In magenta, $Q > 1 \times 10^{-10}\ s^{-2}$ and SLA > + 30 cm or SLA < - 30 cm.

Since this study focuses on identifying intense eddies being generated at the SWIR, only applying a threshold to the Q field does not suffice. From Table 1 (pg 15), strong eddies are generally characterised by having core SLA values in excess of +30 cm for warm

5. GENERAL CIRCULATION AT THE RIDGE.

The dynamic environment around the South-West Indian Ridge is a crucial component in the sustainability of the marine ecosystem of the region. Lying meridionally, the ridge confines the flow of the ACC, inducing its baroclinic instability. Direct hydrographic observations in that region have highlighted both the spatial and temporal nature of the variability (Ansorge and Lutjeharms, 2002, 2005; Ansorge *et al.*, 2006). The inherent limitation of hydrographic data is that it only provides a synoptic snapshot of the circulation at the time of each survey. Suitable monitoring capability is hampered by the difficulty of sampling using conventional ship-borne instruments coupled with the remoteness of the region. The new technological push in establishing a worldwide ARGO float network certainly offers an alternative option to sampling such remote regions. However, the lack of year round accessibility and seasonal extent of sea ice in the Southern Ocean have resulted in this region remaining under-sampled by the ARGO array. Consequently, changes on various timescales in the position of the fronts and their associated volume transport and speed can only be speculated. By contrast, modelling capabilities may provide the key to resolve these questions.

This chapter addresses key question 1, where the general hydrographic setting of the SWIR region is described using the OCCAM model outputs, satellite data and available hydrographic and drifter data. In doing so, it will be possible to compare the reliability of OCCAM (OC-4 and OC-12) against in-situ data as well as better understand the general circulation of this region. Furthermore, the wider-scale circulation pertinent to the dynamics of that region is also discussed. It is anticipated that OC-12 will perform better at representing the dynamics at the ridge.

5.1. Frontal Systems.

Hydrographic sections across the ACC along 30°E and 40°E (CIVA and SWINDEX respectively) have been used as a reference for OCCAM in order to identify the position of the Subantarctic and Antarctic Polar Fronts within the model (Figure 5.1).

eddies and -30 cm for cold eddies. However, in order to aid feature tracking, SLA values greater than +15 cm (and less than -15 cm) were used in conjunction with $Q > 1 \times 10^{-10}$ s^{-2}. Figure 4.6 shows the same SLA field as above overlaid by selection fields [$Q > 1 \times 10^{-10}$ s^{-2}; |SLA| > 15 cm] and [$Q > 1 \times 10^{-10}$ s^{-2}; |SLA| > 30 cm]. The final selection fields shown in Figure 4.6 are slightly more rigorous than that shown in Figure 4.5c. However, they coincide well with the two negative anomalies centred at (48°S, 34°E) and (48.5°S, 38°E). Using this method, it is clear in the example that not all anomalies are potential candidates. For instance, the positive anomaly centred at (49°S, 39°E) is left out.

Feature tracking was undertaken following three predefined rules.

1. Only eddies that have been generated in the vicinity of the ABFZ are considered.
2. Eddies tracked must in their lifetime have reached core-SLA greater than +30 cm (or less than -30 cm).
3. Features are tracked as long as SLA > +15 cm (or < -15 cm) and $Q > 1 \times 10^{-10}$ s^{-2}.

For the purpose of this study, the exact position of an eddy is not essential. The aim is to identify the general path of eddies that are generated at the ridge in order to assess the model's suitability. The position of an eddy, to one decimal place of latitude/longitude, is taken at its core.

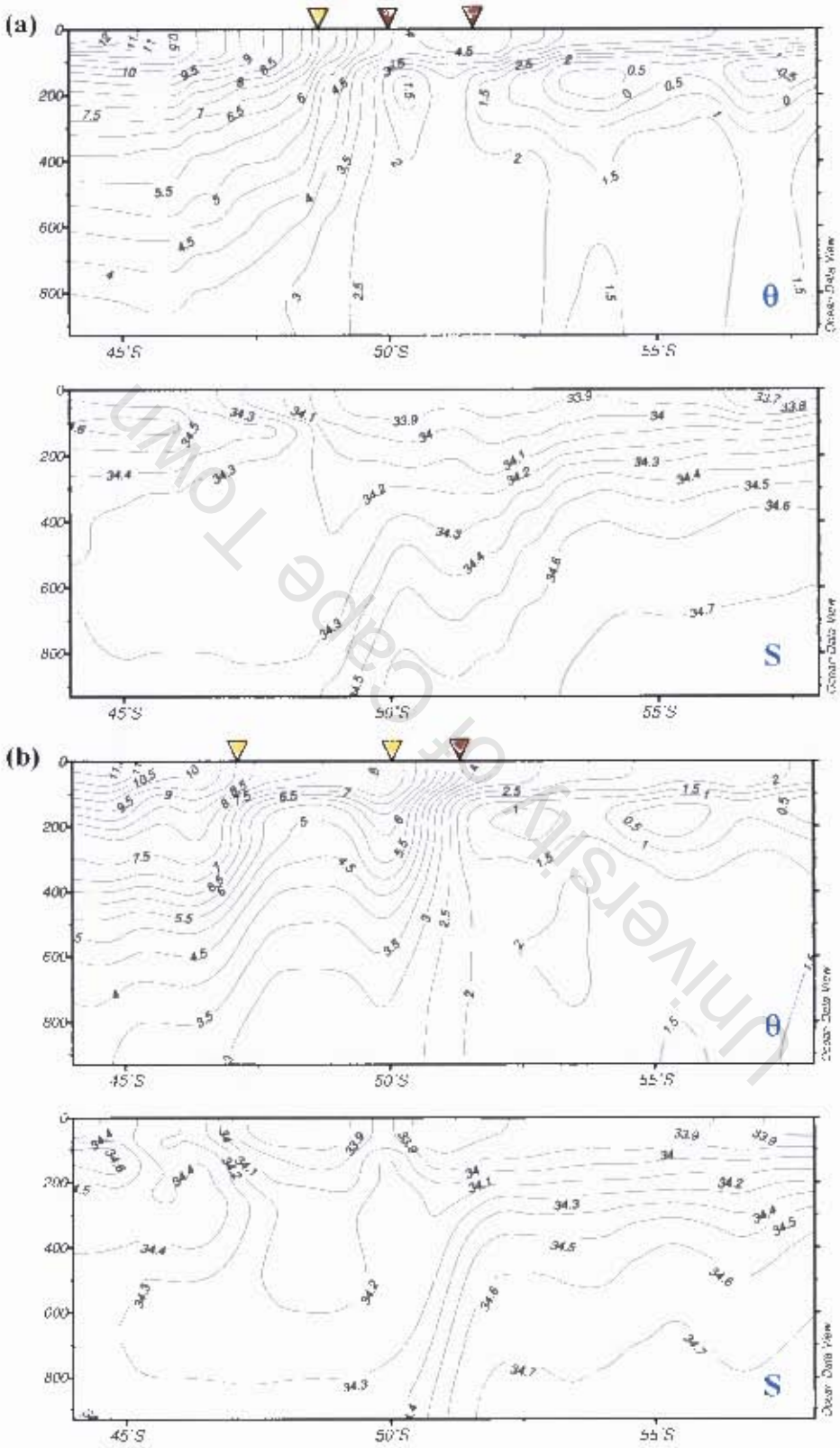

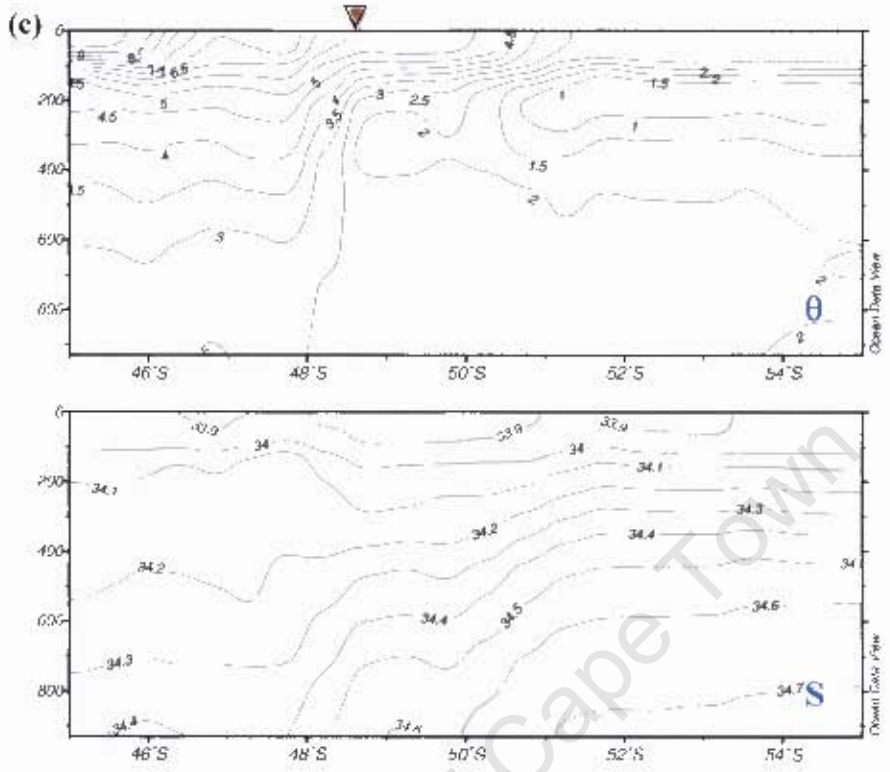

Figure 5.1: Potential temperature and salinity sections of the upper 930 m during three hydrographic cruises (see Figure 4.4): (a) CIVA-1, (b) CIVA-2, both along 30°E between 44 – 58°S, and (c) SWINDEX along 40°E between 45 – 55°S. Temperature sections are contoured at 0.5°C intervals while salinity sections are contoured at 0.1 psu intervals. The positions of the SAF and APF are shown using inverted yellow and brown triangles respectively.

Park *et al.* (1998, 2001) have adopted the following definitions to identify the fronts observed during the repeat CIVA cruises (Figures 5.1a,b). The subsurface position of the SAF was identified using the axial values of 0 = 6°C, S = 34.3 at 200 m (Park *et al.*, 1993) and the APF using the northernmost extent of the 2°C isotherm between 100 and 300 m (Lutjeharms and Valentine, 1984). During the 1993 CIVA-1 cruise, the SAF was observed at 48°S and the APF exhibited a double structure at 50°S and 52°S. The second section undertaken in 1996 highlights both the temporal and spatial variability of the ACC. In contrast to 1993, only a single branch of the APF was observed at 51.1°S, whereas two branches of the SAF were observed at 47.15°S and 50°S. Moreover, the southern branch of the SAF appeared to have merged with the APF. Further investigations by Pollard and Read (2001) upstream of the ridge along 40°E identified the SAF and APF at 44°S and 48.7°S respectively.

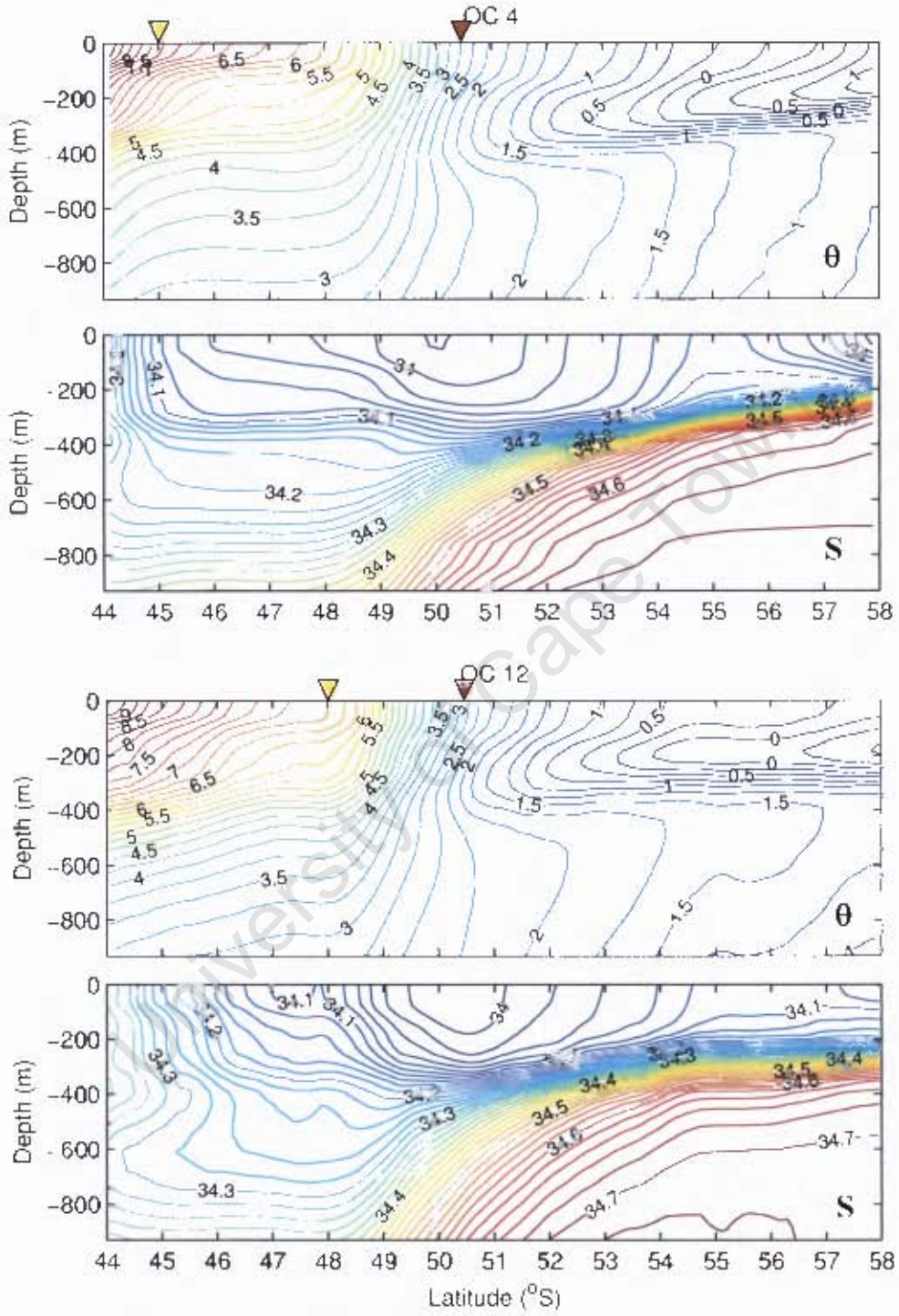

Figure 5.2: Potential temperature (°C) and salinity sections (10-year average) of the upper 930 m in OCCAM (at both resolutions) along 30°E between 44 58°S. Temperature sections are contoured at 0.25°C intervals while salinity sections are contoured at 0.05 psu intervals. The positions of the SAF and APF are shown using inverted yellow and brown triangles respectively.

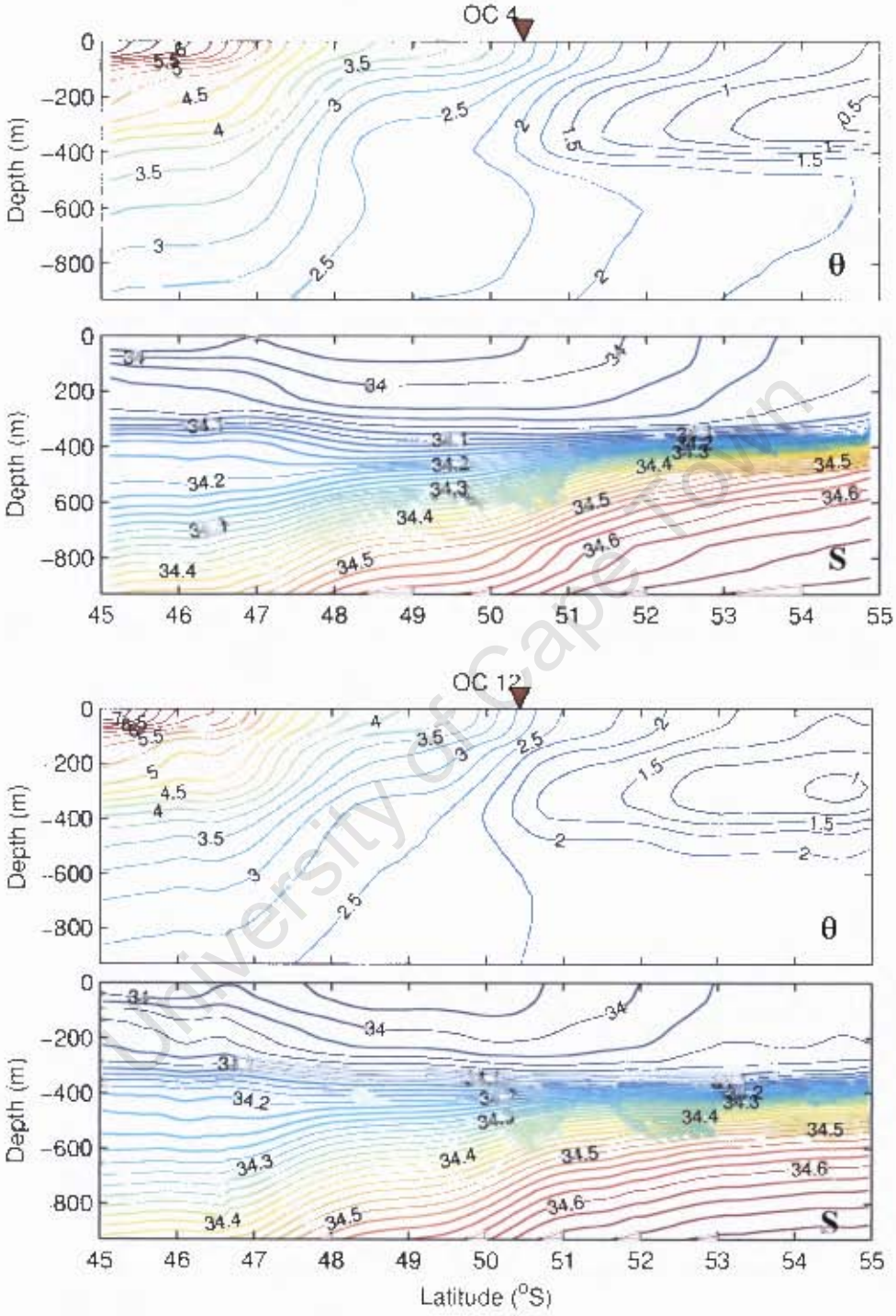

Figure 5.3: Same as Figure 5.2 but along 40°E between 45 – 55°S.

The CIVA-1 and SWINDEX sections were undertaken almost concurrently (March – May 93). Both frontal bands showed a northward deflection along 40°E, the SAF by 4° of latitude and APF by 1.3° – 3°, increasing the width of the Antarctic Polar Frontal Zone.

This epitomises the spatial variability of the ACC. Evidently, the SWIR imposes a distinct barrier to the flow of the ACC resulting in the deflection of the fronts associated with the current.

For reasons of consistency, the same definitions employed by Park et al. (1998, 2001) and Pollard and Read (2001), have been used to identify the geographic location of the SAF and APF within OCCAM. Two 10-year averaged sections along 30°E, between 44 – 58°S, and along 40°E, between 45 – 55°S, were calculated and the results are presented in Figures 5.2 and 5.3 respectively. Only the top 930 m is considered since frontal features are generally easier to identify in the upper layer of the water column where water masses converge or diverge (Whitworth and Nowlin, 1987).

The SAF lies on average at 45°S along the 30°E section in OC-4, while in OC-12, it is found further south, at 48°S. Using the above definition, the APF is identified at 50.3°S at both resolutions. This front, in the temperature section, usually marks the position where the warm subantarctic surface waters ($\theta > 4°C$) meet the relatively colder antarctic surface waters ($\theta < 1°C$). The sudden jump in isotherms associated with the APF is observable throughout the upper 930 m of the water column. South of this narrow intense front, a temperature minimum layer, lying between 100 and 400 m at 58 and 51°S respectively, is capped by a relatively warmer and fresher surface mixed layer.

Along the 40°E section (Figure 5.3), the SAF lies to the north of the section chosen as a result of the deflection at the ridge (Figure 1.2, pg 6). The temperature section is similar to that observed along 30°E, with the APF, on average, lying at 50.4°S at both resolutions and the presence of a subsurface temperature minimum south of 51°S. Throughout the water column horizontal isohalines suggest strong salinity stratification.

At both resolutions, a tongue of temperature minimum waters centred at 200 m along 30°E ($\theta < 0.5°C$) and at 300 m along 40°E ($\theta < 1°C$) is characteristic of Winter Water, residuum of a previous winter mixed layer (Park *et al.*, 1998). This water mass was observed at the mid-depth within the core of a cold eddy in the sub-antarctic (Ansorge *et*

al., 2006). Physico-chemical characteristics of this eddy confirm its source to be from south of the APF (Ansorge *et al.*, 2006; Bernard *et al.*, 2007). This suggest that antarctic eddies crossing the APF into the subantarctic may provide a mechanism for the equatorward transport of Winter Water.

A well-defined halocline, separating the relatively fresher surface water ($S < 34.1$) from water at depth ($S > 34.6$), is noted in both sections south of 50°S. Along the 30°E section, the halocline shoals from 400 to 200 m between 51 and 58°S. Further east, it is observed lying at 400 m. The most prevalent water mass in the Southern Ocean, the Circumpolar Deep Water (CDW), is usually characterised in two distinct cores, namely the Upper CDW, with low oxygen concentration, and Lower CDW, having a salinity maximum (Whitworth and Nowlin, 1987). Some penetration of LCDW is evident along the western section below the halocline.

The three hydrographic sections (Figure 5.1) portray a snapshot of the prevailing conditions at the times of the respective cruises and are, therefore, not proof of any particular pattern. Conversely, it must be noted that the OCCAM sections are 10-year averages and certain features are smoothed out. Eddies and meanders leading at times to double expressions of fronts or even merging of two fronts into a single intense structure (Holliday and Read, 1998; Park *et al.*, 2001; Pollard and Read, 2001), are not resolved in the OCCAM climatic sections. Nonetheless, the OCCAM sections at both resolutions represent the general structure very well although some minor discrepancies are noted, possibly resulting from the underlying inaccuracies in the surface forcing employed in the model coupled with the relaxation of surface salinities towards monthly Levitus values.

5.2. Mean Circulation.

This section studies and compares the average sea surface temperature (SST), near-surface velocity and eddy kinetic energy (EKE) observed from AMSR-E, drifters, altimetry and OCCAM. Once again, OCCAM OC-4 and OC-12 products were in all cases averaged over a period of 10 years.

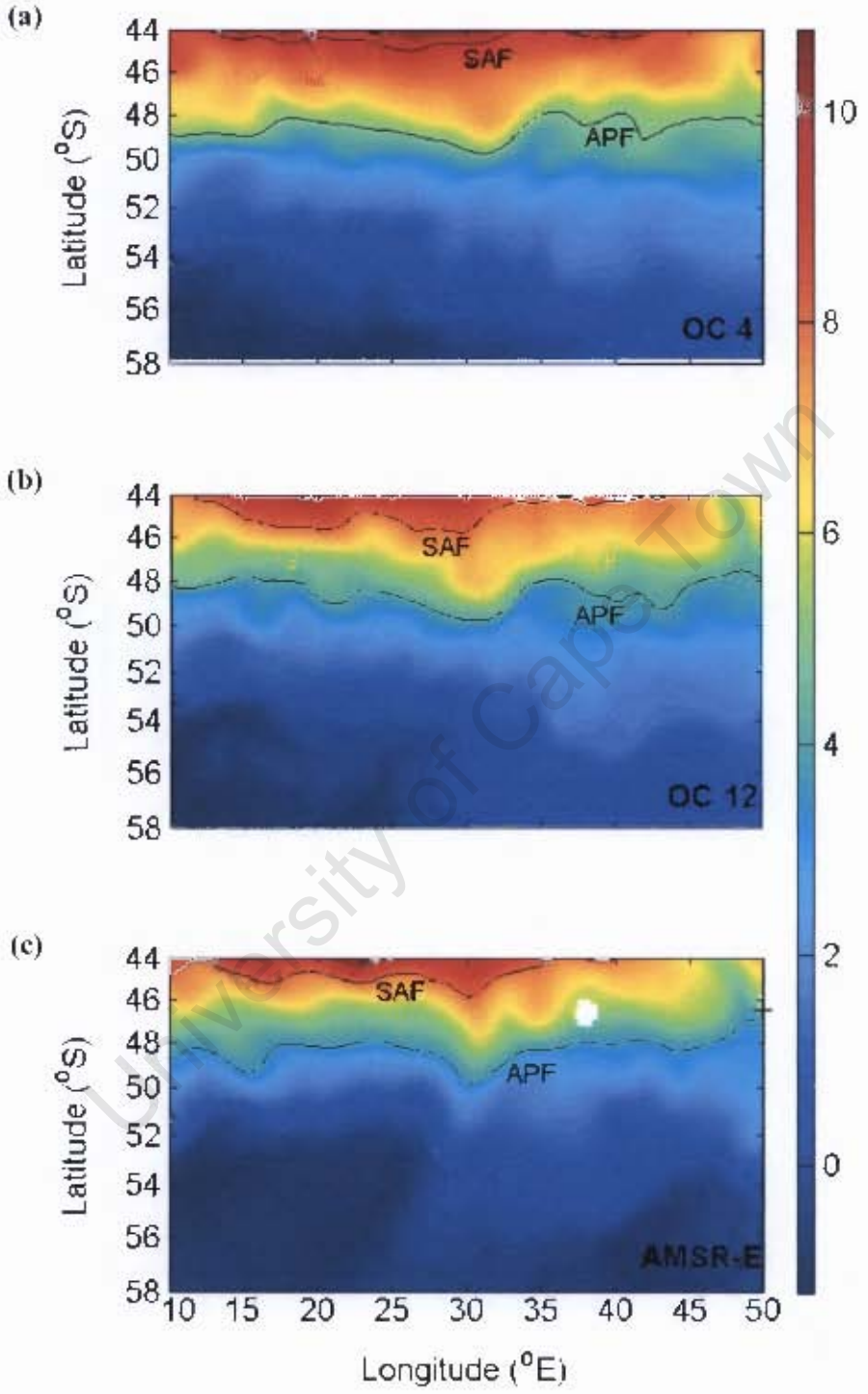

Figure 5.4: Sea surface temperature (°C) from (a) OC-4, (b) OC-12 and (c) AMSR-E. OCCAM products are 10-year averages while AMSR-E plot is an average for the years 2002 to 2006. The blank area seen on the AMSR-E plot corresponds to the location of the Prince Edward Islands. The position of the Subantarctic (8°C isotherm) and Antarctic Polar (4°C isotherm) fronts are overlaid (Definitions of surface expression of fronts follows Lutjeharms and Valentine (1984)).

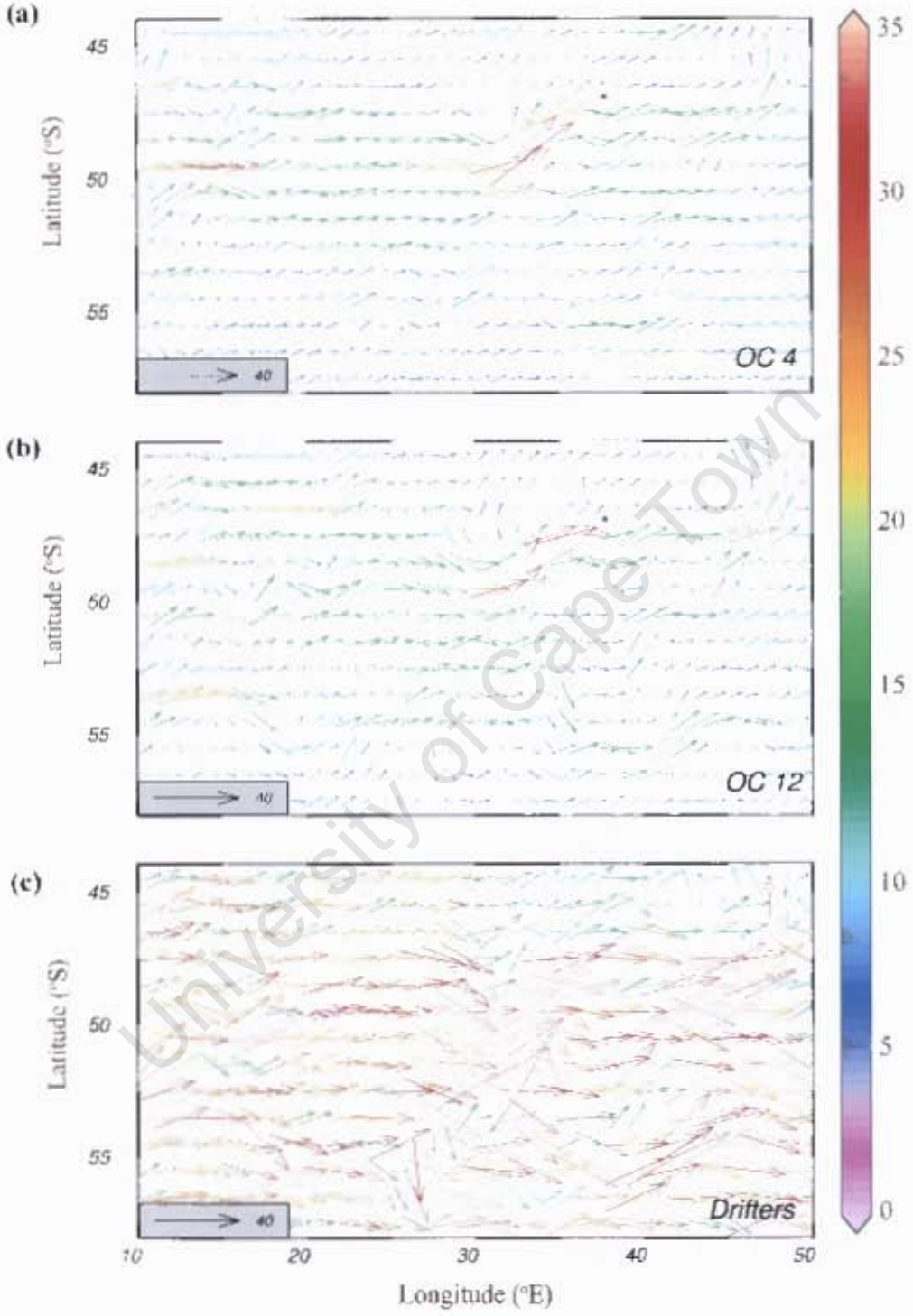

Figure 5.5: Near-surface velocity (cm s^{-1}), averaged over 1° x 1° squares, from (a) OC-4, (b) OC-12, both at 13.7 m (level 3), and (c) drifters drogued at 15 m. OCCAM products are 10-year averages while the drifter plot is an average of all WOCE-GDP data available between 1987 and 2005.

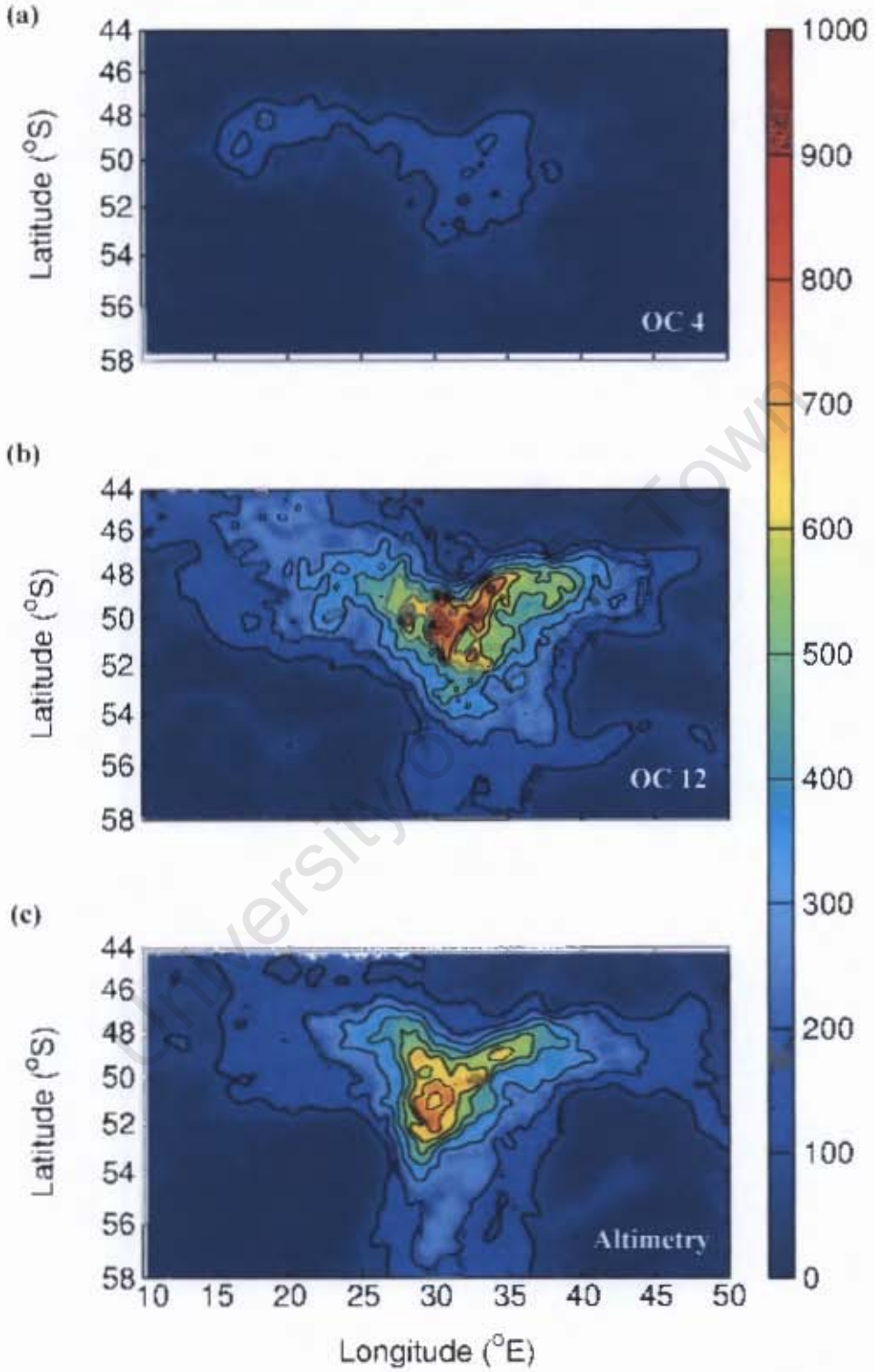

Figure 5.6: Eddy kinetic energy ($cm^2\ s^{-2}$) from (a) OC-4, (b) OC-12 and (c) altimetry. OCCAM plots are averaged for years 1989 1999 and altimetry for years 1992 2006. Contours are drawn at 100 $cm^2\ s^{-2}$ interval.

A 5-year SST climatology was calculated using the AMSR-E microwave dataset (Figure 5.4c). Some striking similarities can be identified in Figures 5.4a-c. Firstly, the position of the APF on average lies along the 49°S latitude in all three cases. Secondly, the channelling and subsequent north-eastward deflection of the APF at the Andrew Bain Fracture Zone (Figure 1.2, pg 6) is well represented at both resolutions in Figures 5.4a,b. And lastly, a tongue of relatively colder surface water jutting across the Antarctic Polar Frontal Zone, between the Del Caño Rise and the Crozet Plateau (Figure 1.2) is shown. Not surprisingly, the coarse resolution of OC-4 output fails to represent in detail the extent of that protrusion along 48°E. The SAF lies further north at this coarse resolution, which was also observed in the section along 30°E (Figure 5.2).

Figure 5.5 shows near-surface velocity vectors averaged over 1° x 1° grids plotted using the same scale. It is evident that, over the region, OCCAM severely underestimates the magnitude of the flow. Drifter velocities are approximately 2.9 (3.3) times higher than OC-4 (12) velocities. Point-wise statistical correlation yields almost no quantitative similarity ($r = 0.32$, $p < 0.05$ at both resolution) between drifter and model observations. The discrepancy may arise as a result of unequal sampling from drifters, both in time and space. Moreover, although windage has been reduced to a strict minimum by using only data from drogued buoys, there may still be some degree of contamination in the recorded velocities due to other factors. Nonetheless, some qualitative similarities are observed. The highest speeds, exceeding 30 cms^{-1} at both resolutions, are located immediately downstream of the Andrew Bain Fracture Zone, along the eastern flank of the SWIR at 33°E. The surface flow between 44 and 46°S along 48°E exhibits a distinct northward deflection, which corresponds to the intrusion of cold water (< 4°C) observed in Figure 5.4. Indeed, this result is comparable to mooring data collected during SWINDEX which identified frequent cold water pulses between the Del Caño Rise and the Crozet Plateau (Pollard and Read, 1997). Pollard and Read (1997, 2001) have estimated the transport to be approximately 30 Sv in the gap west of the Crozet Plateau.

Not only is the mean circulation at the SWIR spatially highly variable, the region is also energetic (on all timescales) as the EKE maps in Figure 5.6 suggest. A confined region

(48–54°S, 25–40°E) of high eddy kinetic energy (> 500 cm^2 s^{-2}, Figures 5.6b,c) is observed amidst a relatively quiescent environment. The variability in OC-4 is significantly less energetic. The largest EKE values exceeding 700 cm^2 s^{-2} in OC-12 and altimetry are located at 50°S, 30°E, corresponding to the location of the Andrew Bain Fracture Zone. In OC-4, however, highest EKE values (~200 cm^2 s^{-2}) is observed further west, along 49°S at 17°E. This may suggest that the shallow bathymetry of the Meteor Rise (Figure 1.2) may also obstruct the flow of the ACC prior encountering the SWIR. Moreover, an enhanced mean flow is further noted in Figure 5.5a at the same location. This peculiar hotspot is not present in OC-12 and altimetry leading to the conclusion that the erroneously high EKE in OC-4 results from of the coarse isobaths defined in the low resolution run of the model.

Of interest in Figure 5.5c, a small region centred at 53°S and 40°E corresponding to the position of the Conrad Rise (Figure 1.2, pg 6), where sub-surface velocities are substantially reduced. The exact cause of this is unclear. Closer inspection of the drifter data reveals two distinct high-velocity jets north and south of the Rise. In the coarser resolution of OC-4, the circulation around the Conrad Rise is poorly represented. OC-12's representation is fairly consistent to the drifter observations although the velocities associated with the defection north and south of the rise are far less than what is observed. What could be the cause of this apparent bifurcation? The shallow nature of the Conrad Rise (< 1500 m) may be acting as a topographical obstacle to the flow of the ACC, forcing it around the Rise. Gouretski and Danilov's (1993) simulation of five jets show that the nature of the meandering in the Enderby Basin is dependent on the physical parameters of their inertial jet model. However, in all cases, their jets converged along the eastern flank of the Conrad Rise showing only a northward deflection. Craneguy and Park (1999) have made similar conclusions. Their results further showed a meandering of the jets in the Enderby Basin, and a subsequent refocusing along the northern flank of the rise closely following the *f/h* contour. Pollard and Read (2001) have called this part of the flow 'the Ob'-Lena Front' and associated with it, through direct measurement, a mean transport of 35 Sv. Based on the low temporal variability in altimetry observations, they proposed that the front is a quasi-permanent feature.

The proposed conjecture of the Conrad Rise forcing the ACC to fragment into two branches north and south may not seem plausible since both inertial jet model studies fail to represent both branches. Yet high velocities on both sides of the rise are observed. It is worth noting that the jets initiated in both studies originated immediately upstream of the Andrew Bain Fracture Zone and are therefore not representative of the whole transport of the ACC. Pollard and Read's observations do not extend south of the rise either. As a result, it is likely that the portion of the flow adjacent to the southern flank of the Conrad Rise is not directly influenced by the SWIR. In the light of these observations, it might be more appropriate to refer to the branches of the flow around the Conrad Rise separately as the North and South Ob'-Lena Front. However, hydrographic data are not available to confirm this. EKE values (Figure 5.6) in the same region are very low corroborating Pollard and Read's (2001) conclusion of the low variability at the Rise. The variability of the southern branch, in OC-12, is slightly more energetic (100 – 200 $cm^2\ s^{-2}$) than its northern counterpart (< 100 $cm^2\ s^{-2}$). Current investigations looking at drifter, float, altimetry and model data provide further details about the bifurcation of the ACC at the Conrad Rise (Durgadoo *et al.*, submitted)

5.3. Conclusions.

The time-average flow associated with the SWIR and the ability of OC-4 and OC-12 to accurately represent the circulation have been scrutinised in this chapter. The structure of the upper water column along two meridional sections was analysed and compared to hydrographic data available along these sections. The sea surface temperature, near-surface velocities and eddy kinetic energy were also examined and comparisons were drawn between model and observed outputs.

Notwithstanding OC-4's representation of the SAF, which was identified further north, the mean positions of the SAF and APF over the SWIR at both resolutions satisfactorily agree with previous findings of Lutjeharms and Valentine (1984) and Holliday and Read (1998). The mean circulation at the SWIR in the model as seen in the three fields (Figures 5.4–5.6) further demonstrates the validity of the model's simulation, especially at $^1/_{12}^o$.

This is despite the fact that the model underestimates the near-surface velocities to a large extent. Both the mean and eddy flow in the SWIR region is variable and seemingly unpredictable. Moreover, the magnitude of the eddy kinetic energy and its geographic distribution in OC-12 is comparable to that observed from altimetry data. This conclusion provides an indication that OC-12 may also adequately represent the turbulent nature of the variability, which is known to be predominantly in the form of meanders and eddies. OCCAM's depiction of the general circulation at the ridge (key question 1) is satisfactory. Consequently, the OC-12 outputs can be used with adequate confidence to investigate and map the role the SWIR has on eddy genesis and trajectory.

6. MESOSCALE FEATURES WITHIN THE MODEL.

It has been shown (Ansorge and Lutjeharms, 2005) that eddies and meanders occur as a result of the ACC's interaction with local shallow bathymetry. Because of the ecological importance of mesoscale eddies (Jonker and Bester, 1998; Nel *et al.*, 2001) in providing a mechanism for the cross-frontal advection of biological organisms (Bernard *et al.*, 2007) at the South-West Indian Ridge, it is imperative that the model accurately simulate this particular aspect of the variability (key question 2). The general circulation at the ridge is better represented in OC-12 (chapter 5). Therefore, SLA maps have been calculated only using OC-12 outputs and features are tracked as per the three criteria described in section 4.5.2. Restrictions imposed on identifying and tracking anomalies have been established from observed behaviour and values (Table 1, pg 15) associated with eddies at the SWIR. Furthermore, the well-established assumption that sea surface height anomalies correspond to mesoscale hydrographic eddies in the model has been made following results by Ansorge and Lutjeharms (2000, 2003, 2005). Results are compared with a comprehensive study by Ansorge and Lutjeharms (2003), whose work has described and quantified sea level anomalies generated at the ridge from TOPEX/ERS altimetry products.

6.1. Identifying mesoscale eddies from SLA fields.

Twenty two anomalies identified within OC-12 were tracked over 10 years (Figure 6.1). In all cases, the anomalies reached a minimum SLA magnitude of at least 30 cm, which has heuristically been defined as being intense in that region (Pakhomov *et al.*, 2003; Ansorge and Lutjeharms, 2005). Tracking commenced when anomalies reached SLA magnitude of 15 cm and ended when they decayed to the same value. In some cases, the anomalies appear to either merge with other features or split into two distinct features, yet remaining recognisable from their SLA signature. This made positioning of the anomalies ambiguous. In these instances, the overlaid Q-fields were used as the final arbiter. Merging and splitting of anomalies usually resulted in a loss of potential vorticity and therefore falling below the $Q = 1 \times 10^{-10}$ s^{-2} threshold. The tracks were either terminated

or continued provided the Q and SLA thresholds were still satisfied. Features in OCCAM are unlikely to disappear from one time frame to the next due to the even spacing of data points in the model and the grid resolution which, over the SWIR domain in OC-12, is on average 9.3 x 5.8 km. The diameter of a typical eddy is of the order of 100 km (Table 1) and thus should be represented by about 145 data points in the model at that resolution.

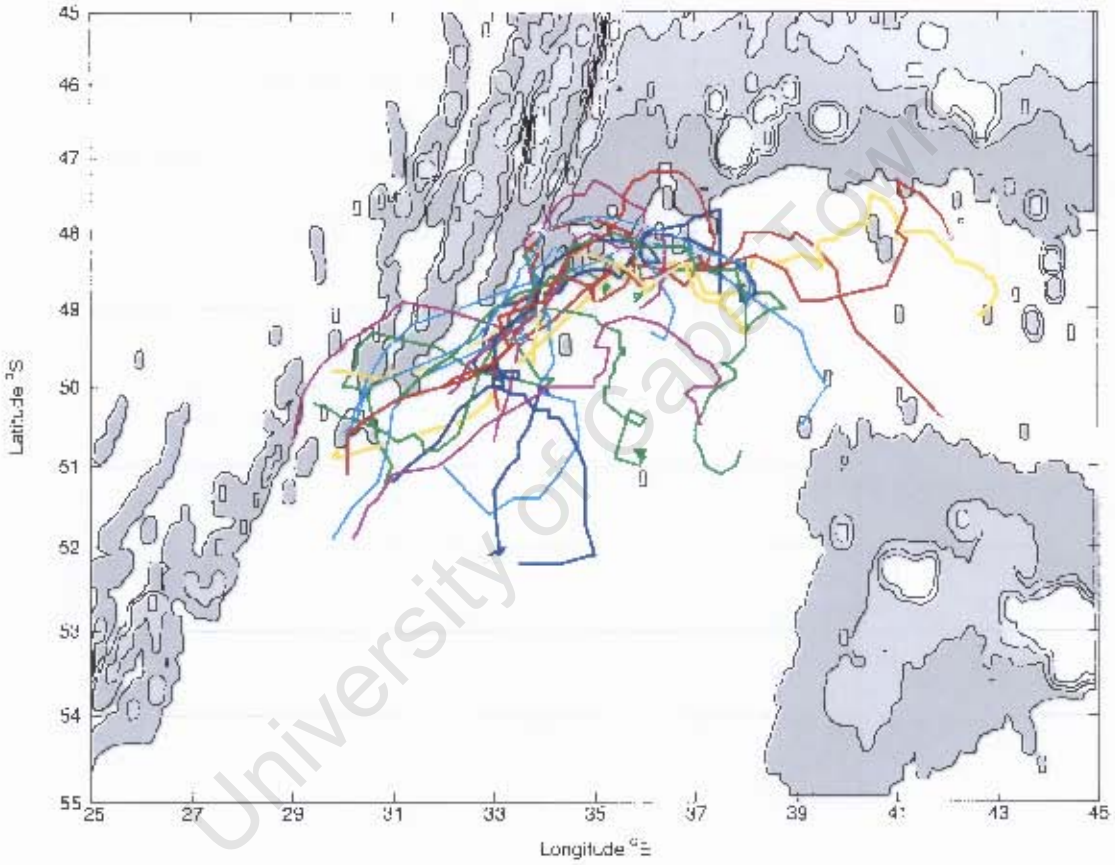

Figure 6.1: Trajectories of 22 anomalies (2 positive, 20 negative) tracked in the 10-year OC-12 dataset. The magnitude of the f/h contours (0.1 – 0.4 rad s^{-1} m^{-1}) are shown at 0.1 rad s^{-1} m^{-1} interval. The tracks closely follow the f/h = 0.4 contour between 32°E and 37°E.

The trajectories of the 22 intense anomalies show some degree of coherence. The general pattern agrees well with previous observations (Ansorge and Lutjeharms, 2003). The anomalies, generated immediately east of the Andrew Bain Fracture Zone (30 – 33°E), travel in a north-eastward direction following the eastern flank of the ridge until 37°E. Thereafter, they drift eastward where some meandering is also observed. Remarkably, between 32°E and 37°E, the anomalies closely follow the f/h = 0.4 rad s^{-1} m^{-1} contour.

Thereafter, the strong topographic influence on the trajectories seems to be lost. The anomalies appear to be confined within a small area. It is likely that the anomalous water properties associated with the eddies would eventually disperse within the confined corridor. A similar hypothesis has been put forward following the detailed description of an intense cold eddy surveyed in the Antarctic Polar Frontal Zone in 2005 (Ansorge *et al.*, 2006; Swart *et al.*, 2008).

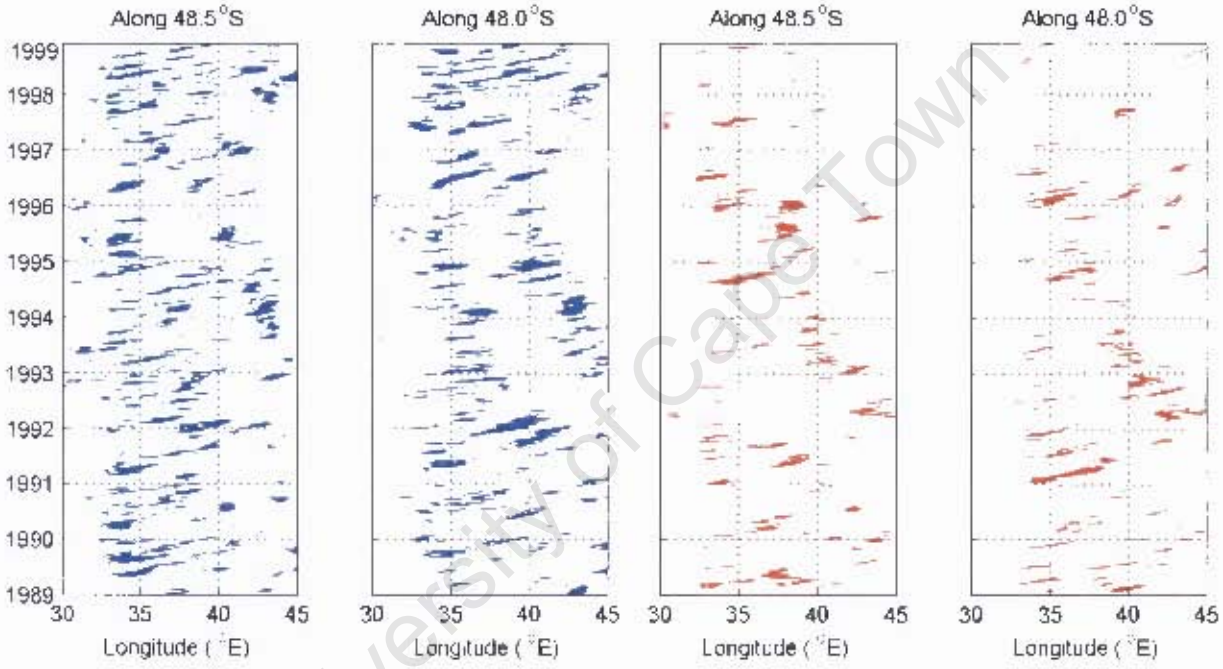

Figure 6.2: Temporal hovmuller plot along 48.5°S and 48°S showing the propagation of negative (blue) and positive (red) anomalies using the SLA| > 15 cm and Q > 0 s^{-2} criteria.

Only two of the 22 anomalies tracked were positive. Surprisingly, the model generated fewer warm eddies than anticipated. In their survey using 5 years of altimetry data, Ansorge and Lutjeharms (2003) identified on average equal number of positive and negative anomalies being spawned at the ridge. There may be several possible reasons for this discrepancy. Warm eddies typically originate north of the SAF (Ansorge and Lutjeharms, 2005). With the mean northward deflection of the SAF within the model (section 5.1) upon encountering the ridge, the likelihood of warm eddies being spawned in the vicinity of the ABFZ is slim. Nevertheless, owing to the variable behaviour of frontal systems in that region, more than two positive anomalies should be observed in a

10-year dataset within the model. Ansorge and Lutjeharms (2003) systematically tracked their anomalies manually. The criteria they use to locate and track features were different to that used in the present study, which focuses on high-amplitude and persistent anomalies only. It is, therefore, possible that anomalies tracked by Ansorge and Lutjeharms might have represented well-defined eddies as well as incipient ones. The disparity between positive and negative anomalies within the model can be further explained by the SLA and Q selection fields, which may have been too stringent and consequently leaving out positive features.

	Mean / Std-Dev	Range
Longevity (months)	4.89 ± 2.20	2 – 10
Distance travelled (km)	783 ± 303	290 – 1420
Advection speed (km/day)	5.51 ± 1.57	1.89 – 8.61

Table 3: Values describing the behaviour of the 22 anomalies tracked at the South-West Indian Ridge within OC-12 (Figure 6.1). These values are commensurate with direct hydrographic observations as presented in Table 1, pg 15.

The mean trajectory of the eddies beyond 34°E is mostly eastward (Figure 6.1). Therefore, two zonal time-longitude (hovmuller) plots along 48.5°S and 48°S, depicted in Figure 6.2, show the propagation of both positive and negative anomalies having |SLA| > 15 cm. It is important to note that the threshold for the parameter Q has been relaxed to Q > 0 s^{-2} (positive distinguishes rotation over deformation) to account for the meandering advection of some eddies. This temporal record shows, especially after 1996, that the number of lasting positive anomalies is substantially less than negative ones. This occurs despite having reduced the threshold for Q to the strict minimum. A few long-lived features (> 7 months) are observed. Furthermore, some features seem to be stagnant for at least 4 – 6 months. It is acknowledged that the mean flow plays a central role on eddy characteristics and vice versa (Stammer, 1998; Hughes and Ash, 2001). Indeed, the trajectories of the features in Figure 6.1 follow the average flow shown in the sub-surface velocity map, Figure 5.5b. Additionally, over the same path, the eddy variability (Figure 5.6b) is high suggesting a strong synergism between the mean and eddy fields at the SWIR. To understand the precise mechanism leading to the observed behaviour of the anomalies in Figure 6.2, the governing relationships between the mean flow and

mesoscale eddies need to be further investigated; subject which is beyond the scope of this study. Nevertheless, several clear conclusions can be made about eddies spawned at the ridge. First, an average of 2 – 3 (strong) anomalies is observed per year between 33 – 40°E within the model. Second, very few features are present east of 43°E, consistent with previous knowledge (Ansorge and Lutjeharms, 2005). And finally, a slight acceleration in the advection of the anomalies is noted along 48°S (as suggested by the curved patterns).

In order to describe the 22 eddies tracked within the model further, characteristic values were computed (Table 3). On average, the simulated mesoscale eddies are short-lived; with longevities of only 4.89 ± 2.20 months (see also Figure 7.1b, pg 62) and travelling at 5.51 ± 1.57 km day^{-1} over a distance of 783 ± 303 km. Morrow et al. (2004a) have pointed out that features shed meridionally across zonal currents, like the ACC, tend to be quickly re-absorbed into the mean flow. The values in Table 3 are reasonably commensurate with direct hydrographic observations at the ridge following the DEIMEC cruises (Table 1, pg 15). Ansorge *et al.* 2006 have suggested that the SWIR region could be a potential source of meridional cross-frontal (APF) heat and salt pump in the Southern Ocean. Accordingly, with an average of 2 – 3 intense eddies crossing the APF per year and travelling across 3 degrees of latitude, it is indeed likely that the turbulence observed at the ridge has consequences reaching beyond sustaining the local ecology.

6.2. Vertical Structure.

To date, the vertical extent of eddies in the Antarctic Polar Frontal Zone in the vicinity of the Prince Edward Islands has not been fully resolved. The negative anomaly during DEIMEC IV was the only eddy to be thoroughly surveyed hydrographically. However, it emphasised the need for deeper stations in order to fully adjudicate the anomalous heat and salt contents of such intense eddies. Limited available ship-time, logistical, mechanical and weather restrictions impede such comprehensive study and consequently, also limits our understanding of how these localised eddies meridionally transport their atypical heat and salt content. Furthermore, it is likely that the number of intense eddies

shed at the ridge vary seasonally, interannually or on a longer timescale. Hence, the net transfer of seawater properties equatorward or poleward would also vary on these timescales. It is therefore important to assess the vertical structure of eddies within OCCAM in the hope of potentially using the model results to address the above questions.

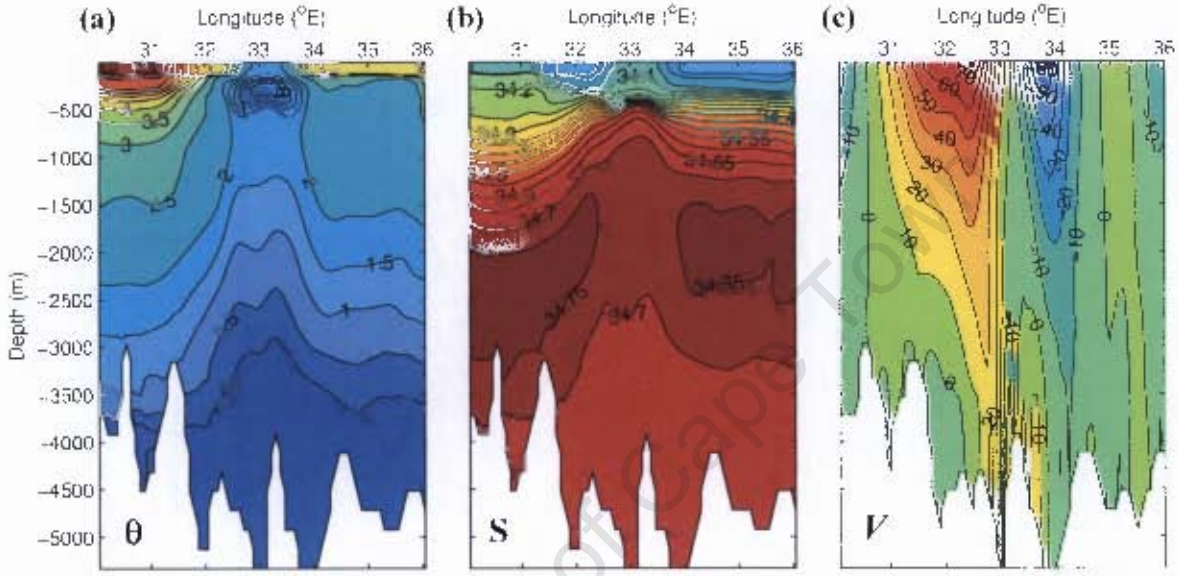

Figure 6.3: Full-depth zonal section along 50°S (between 30 – 36°E) showing the vertical structure of a negative anomaly: Isolines of (a) potential temperature, (b) salinity and (c) full-depth velocity *v*, are contoured at 0.5°C, 0.05 psu and 10 cms^{-1} intervals respectively. The blank portions indicate the local topography.

A zonal snapshot section across a typical cold eddy centred at 50°S, 33°E during model day 2660 is shown in Figure 6.3. This particular eddy, approximately 110 km in diameter, has a strikingly distinct subsurface temperature minimum core ($\theta < 0$°C) at 350 m, which is capped by a well-mixed surface layer which is relatively colder and slightly more saline than the ambient waters. A strong halocline is observed at 500 m marking the boundary between the temperature minimum core and deep water. Salinity distribution within the anomaly increases sharply with depth from 34.1 to 34.7 until 1000 m. Thereafter, a thick homogenous layer of deep water (S ~ 34.7 – 34.75) is observed between 1000 and 2500 m. In contrast, temperature within the anomaly below 1000 m gradually decreases, but yet maintains a ~0.5°C difference with the immediate surroundings. The salient shoaling of temperature and salinity isolines is indicative of an upwelling of deeper waters, which is characteristic of cold eddies. Full-depth velocity in

the *v*-direction shows a well-defined clockwise rotation with velocities at the edges of the eddy exceeding 50 cm s^{-1}, decreasing to ~0 cm s^{-1} at the centre. The western edge of the eddy, with higher velocities, is broader and deeper than the eastern edge. This indicates a net eastward/north-eastward advection of the feature, reinforcing the velocities at the western edge. There is a gradual decrease of velocities with depth until ~2500 m where the rotation at the centre is reversed. Hence, this indicates that, according to the model, an eddy at the SWIR can reach depths up to 2500 – 3000 m and surveying the upper 1000 m hydrographically can indeed be inadequate, nonetheless useful in many cases. These results are generally in good agreement with cold eddies hydrographically surveyed in that region (Koshlyakov *et al.*, 1985; Ansorge *et al.*, 2006; Swart *et al.*, 2008; Figure 6.4) and in other parts of the Southern Ocean (Joyce *et al.*, 1981; Morrow *et al.*, 2004b).

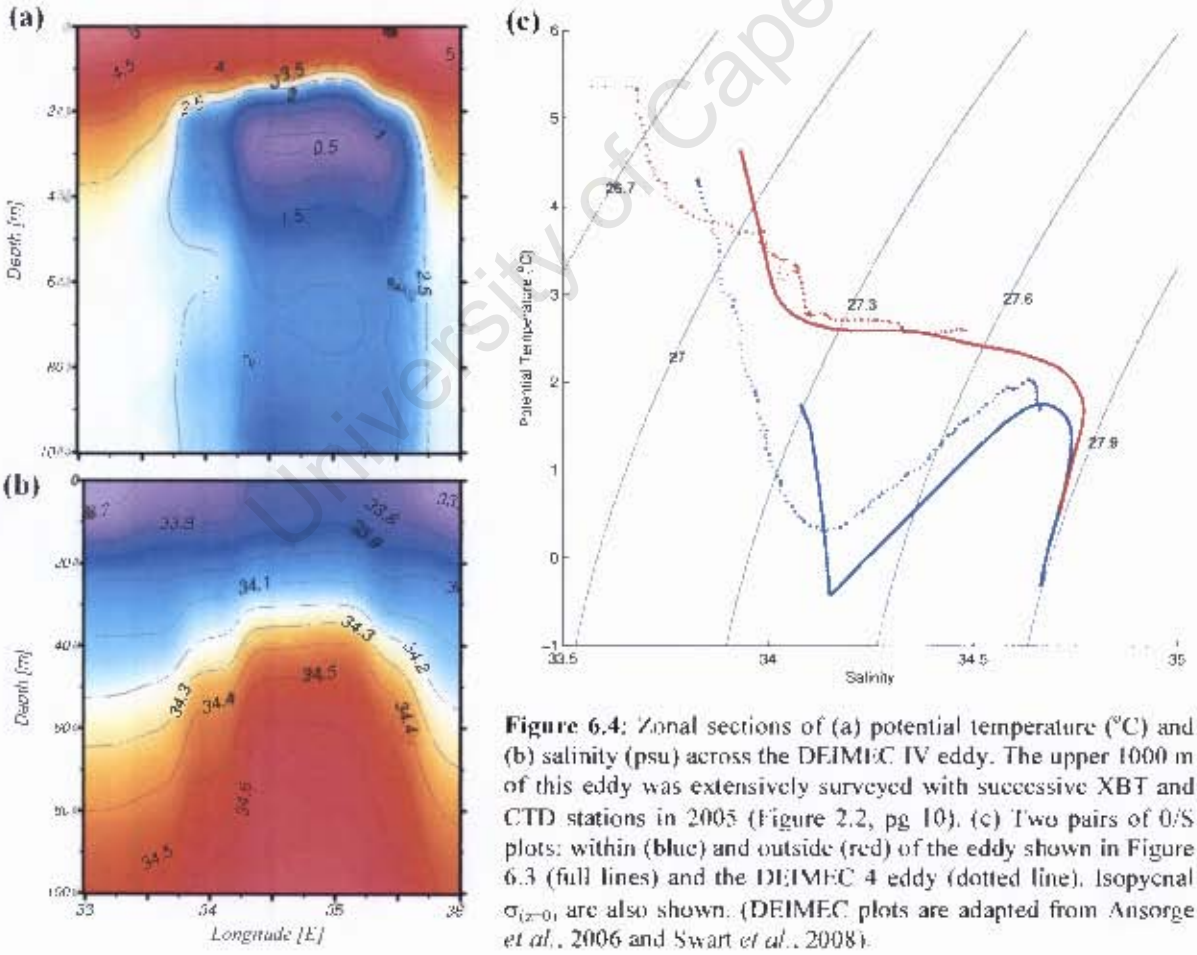

Figure 6.4: Zonal sections of (a) potential temperature (°C) and (b) salinity (psu) across the DEIMEC IV eddy. The upper 1000 m of this eddy was extensively surveyed with successive XBT and CTD stations in 2005 (Figure 2.2, pg 10). (c) Two pairs of θ/S plots: within (blue) and outside (red) of the eddy shown in Figure 6.3 (full lines) and the DEIMEC 4 eddy (dotted line). Isopycnal $\sigma_{(z=0)}$ are also shown. (DEIMEC plots are adapted from Ansorge *et al.*, 2006 and Swart *et al.*, 2008).

Mesoscale eddies provide a mechanism for water mass transport. In particular, following the discussion in the previous paragraph, the eddy shown in Figure 6.3 exemplifies an eddy of antarctic origin in the Antarctic Polar Frontal Zone similar to DEIMEC IV (Figures 6.4a,b). The anomalous temperature/salinity content of this eddy relative to its surrounding is highlighted in Figure 6.4c. The θ/S profiles illustrate the distinct difference in properties at the centre of the feature from the ambient waters. The surface water within the eddy is characteristic of Antarctic Surface Water with temperatures decreasing with from 1.7°C to –0.5°C at almost constant salinity of 34.15. Below this layer lies a temperature minimum core (θ = –0.5°C, S = 34.2) typical of Winter Water (Park *et al.*, 1998). Circumpolar Deep Water is thereafter identified between 1000 and 3000 m (Figure 6.3). The θ/S properties of the ambient water are in stark contrast from those within the eddy. Surface water in the Antarctic Polar Frontal Zone, between the SAF and the APF, consists of gradually modifying Subantarctic and Antarctic Surface Waters. Deep water in this transitional zone is marked by an increasing salinity signature from 34.4 to 34.7, at almost constant temperature of ~2.3°C. In both profiles, a bow-shaped salinity maximum, found at $\sigma_0 \sim 27.85$, marks the location of the Lower Circumpolar Deep Water (Whitworth and Nowlin, 1987) and delimits the depth at which the difference in properties between the eddy and its surroundings becomes negligible.

For comparison, two profiles from DEIMEC IV are also shown in Figure 6.4c. The DEIMEC profiles only extended to 1000 m while the model profiles are full-depth. There are clear similarities between each profile pairs. An offset is observed in the profile pair within the respective eddies. Here, it is important to note that the simulated eddy and the DEIMEC IV eddy were sampled at different stages of their lives. Nevertheless, from both profile pairs, it is evident that water properties within a cold eddy are significantly different from its immediate surrounding. This difference is not only observed at the surface and sub-surface but throughout the entire feature. Therefore, in order to fully resolve the anomalous heat and salt content of eddies traversing the Antarctic Polar Frontal Zone, it is necessary to consider eddies as complete entities.

6.3. Conclusions.

Having established that the general circulation is sufficiently well represented by the model (chapter 5), this chapter has examined the presence and behaviour of mesoscale features within the model in a way that is pertinent to that region, hence addressing key question 2. Ten years of 5-day-mean SLA maps from OC-12 were used to identify and track strong anomalies, ensuring that the distinction between vortices and meanders was made throughout. The focus is set on high amplitude anomalies (> +30 cm or < -30 cm; section 4.5.2) only. The only other work of this kind, undertaken by Ansorge and Lutjeharms (2003) who altimetrically located and tracked anomalies, was used for comparison.

Twenty two intense anomalies were identified, 20 of which were negative and only 2 positive. The lack of warm eddies being generated in the model is unexpected as previous work (Ansorge and Lutjeharms, 2003, 2005) have suggested roughly equal number of positive and negative anomalies in that region. In addition to the different selection process adopted by Ansorge and Lutjeharms (2003), the rigid criteria used in the present study may have contributed towards the apparent lack of warm eddies generated at the SWIR within the model. Nonetheless, the trajectories of the anomalies were observed to follow a clear pattern mainly influenced by the potential vorticity f/h contours. A few stagnant anomalies were observed in a time record. Moreover, certain anomalies seem to last longer than others. The connection between the background mean flow and eddy activities at the SWIR is acknowledged but not entirely understood. Eddies crossing the near-zonal APF carry and dissipate their anomalous heat and salt content within a limited area. A case study of the vertical structure of an anomaly yielded promising results. It is therefore possible to further investigate with reasonable confidence the short and long term impact of eddies spawned at the ridge within the model (OC-12). In particular, addressing the question of how eddies change with age is now possible.

7. DECAY OF EDDIES.

It has been argued in previous studies (e.g. Bernard *et al.*, 2007) and substantiated throughout the last two chapters that eddies at the South-West Indian Ridge have the potential to provide a means of transport for biological organisms across the Antarctic Polar Frontal Zone. This in turn offers an abundant foraging ground for higher trophic consumers of the Prince Edward Islands. Water masses within eddies are distinctly different from ambient waters (section 6.2) thus enabling the organisms they carry to remain in their natural environment while being geographically relocated. Relatively straight-forward identification and tracking of eddies has been made possible by looking at sea level anomaly maps derived from an array of satellite altimeters or from numerical models. It is now widely accepted that features present in the SLA fields do indeed represent hydrographic eddies, to such an extent that the words 'anomalies' and 'eddies' are sometimes used interchangeably. Several sea-going expeditions over the years have successfully demonstrated the collocation of sea level anomalies and hydrographic eddies. Undoubtedly, using the SLA signature of features, several conclusions can be made about the behaviour, pathways and frequency of eddy occurrences in any given location. Furthermore, the spatial and temporal evolution of an eddy has often been inferred by the increase/decrease in its SLA signature. However, the status of an eddy can also be monitored by (1) the strength of its rotation, (2) its anomalous heat and salt content and (3) the shift in its thermocline.

A few mechanisms act together in the gradual erosion of a mesoscale eddy. The upper layer is subjected to active air-sea exchanges (Williams, 1988), hence contributing to the weakening of its surface temperature and salinity signatures. Lateral exchange of properties with the surrounding environment, usually by means of double-diffusion and interleaving, further contributes to the dissipation of anomalous heat and salt content of the feature. These mechanisms also may have a seasonal variation. In addition, the merging or splitting of a feature enhances or lowers its SLA signature. Local bottom topography further influences the intensity and trajectory of a feature. In the previous chapter, it has been shown that eddies at the SWIR on average tend to follow closely *f/h*

contours (Figure 6.1, pg 53). Thus, in all likelihood, bathymetry plays only a minor role in the decay of the features originating at the SWIR. The decay of eddies is evidently a complex process and is expected to vary largely amongst individual features. This chapter addresses the final key question by looking at the change in some physical properties of cold eddies as they age, in particular, their SLA signature, full-depth velocity and anomalous temperature and salinity.

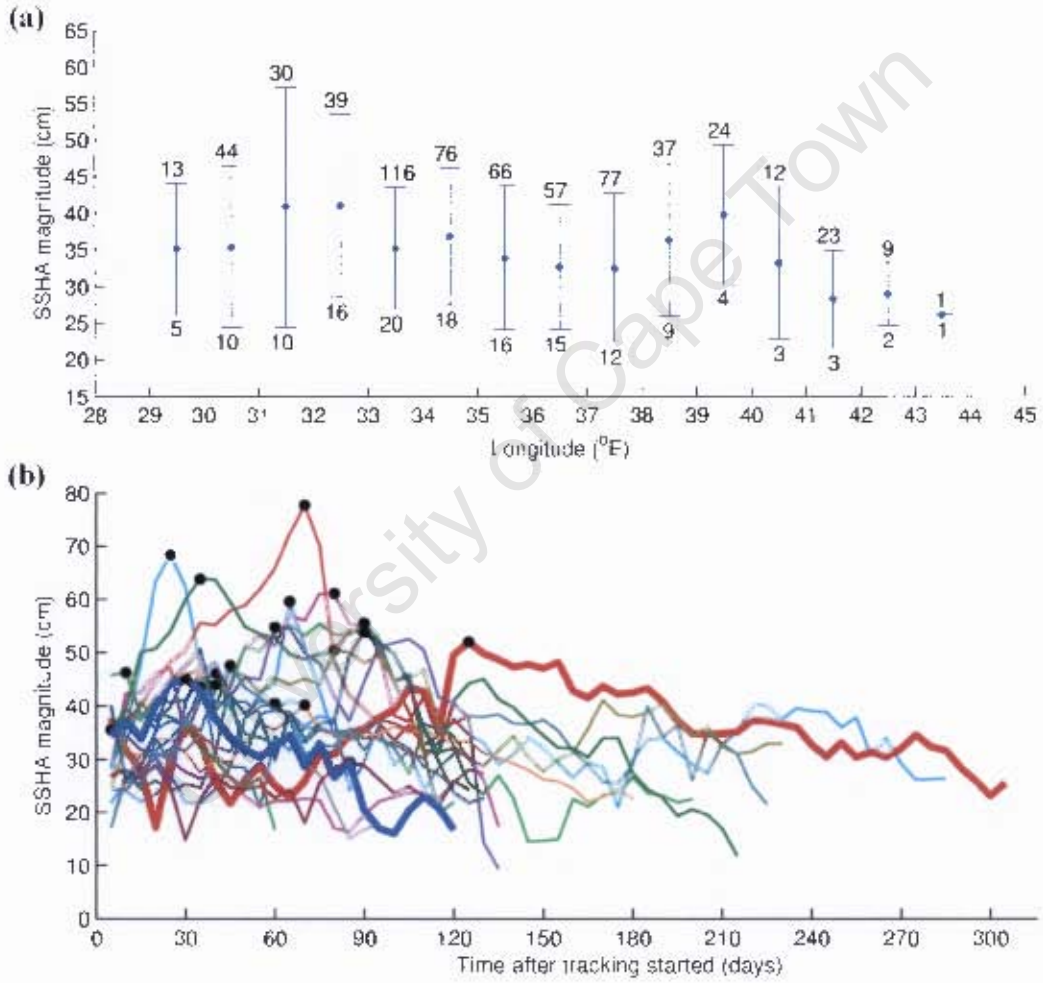

Figure 7.1: The decay in sea surface height anomaly (magnitude in cm) of 20 simulated cold eddies tracked at the South-West Indian Ridge (Figure 6.1, pg 53). (a) Decay with longitude – mean (dots) and standard deviation (error bars) in SSHA. The values above the error bars indicate the number of observations used to calculate the mean and standard deviation per degree longitude, while those below the error bar indicate the number of cold eddies (out of 20) reaching that longitude. (b) The temporal evolution of SSHA – dots indicate the time after generation for each eddy to reach its maximum intensity. The evolution of two eddies is highlighted with thick lines: Eddy 5 in red (Figure 7.2) and Eddy 21 in blue (Figure 7.3).

7.1. Temporal and Geographical Evolution of Eddies.

In Figure 6.1 (pg 53) most of the simulated eddies have spun down before reaching 39°E. Only three features are observed travelling east beyond 41°E. Ignoring the two positive anomalies, the decay in sea surface height anomaly (SSHA a.k.a. SLA) of the features with longitude is presented in Figure 7.1a. At inception between 31 – 33°E, the simulated eddies have the largest variability in SSHA. More than 75% of the features are observed to have travelled between 33 – 37°E. A peak in mean SSHA values (~40 cm) between 39 – 40°E is noted, but with the decreasing number of observations available beyond 38°E, this local maximum is not likely to be statistically significant. Complementing the above, the temporal evolution of the SLA of the 20 features is shown in Figure 7.1b. It is obvious that each individual eddy is distinctly different. On average, the initial generation period is approximately 1 – 2 months. During that time, an eddy evolves into a fully-fledged isolated feature with an overall increasing SLA signature. A broad range of maximum intensities is noted and most eddies reach their peak intensity between 45 and 75 days after genesis. Some eddies exhibits a second peak during their eastward journey into the Enderby Basin. Most features undergo a decay period of about 3 months which is characterised by a gradual decrease in their SLA signature. Of interest, two eddies in this dataset are shown to have reached peak SLA exceeding -65 cm. A subsequent abrupt decay is observed soon after reaching their maximum intensities.

7.2. Eddy Decay – Case Studies.

Figures 7.2 and 7.3 present case studies of two eddies tracked within the model, Eddy 5 and 21 respectively. Zonal sections of potential temperature, salinity and meridional velocity across each eddy at three different stages of its life are shown. In addition, a θ/S plot, showing the change in the water mass at the core of the feature, and the complete track extracted from Figure 6.1 (pg 53), are shown. The general characteristics of the vertical structure of a typical eddy have been discussed in section 6.2 and the following will therefore only highlight the differences pertaining to the decay of the two features. It is important to note that, tracking of all eddies started at location A and ended at point C,

where it could no longer be unambiguously identified using the combination |SLA| > 15 cm and $Q > 1 \times 10^{-10}\ s^{-2}$.

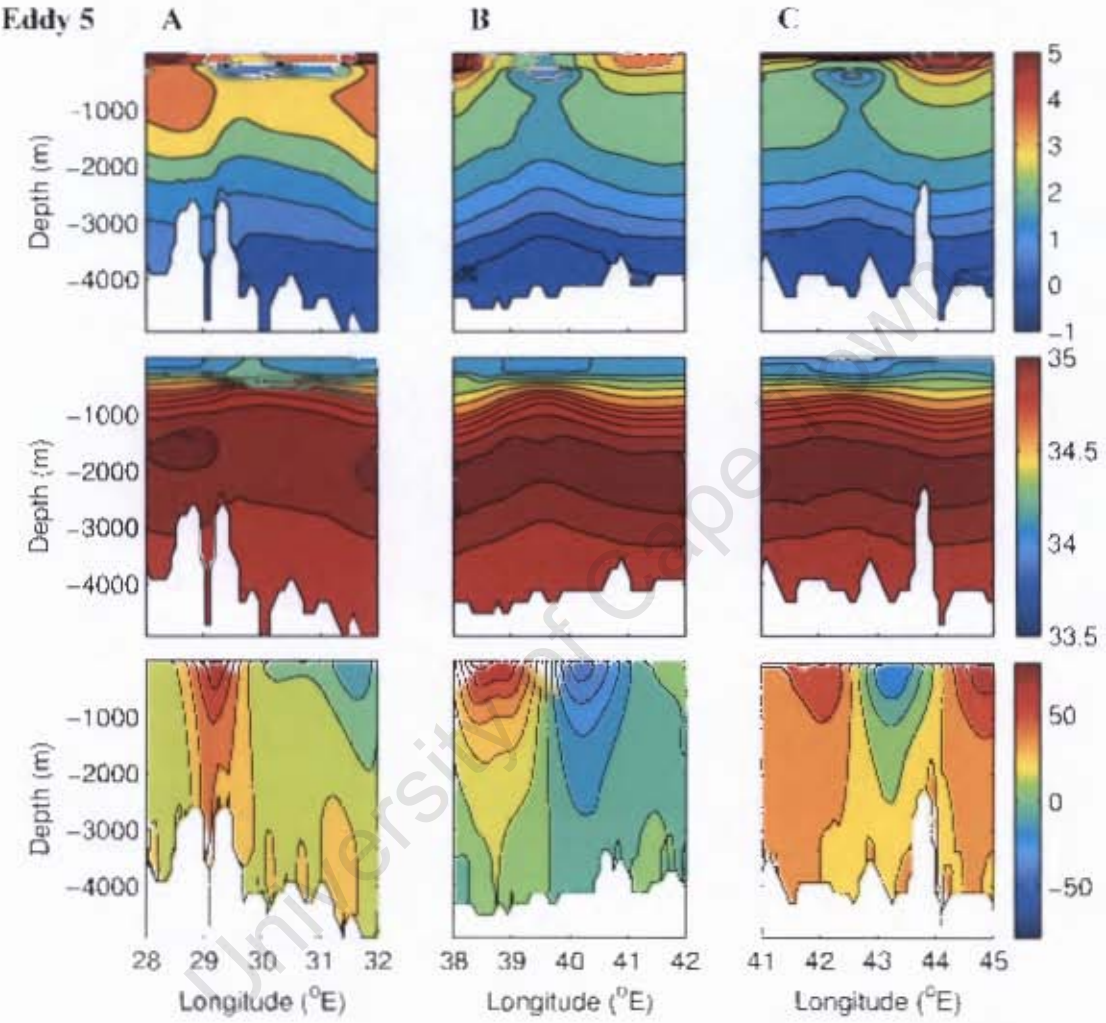

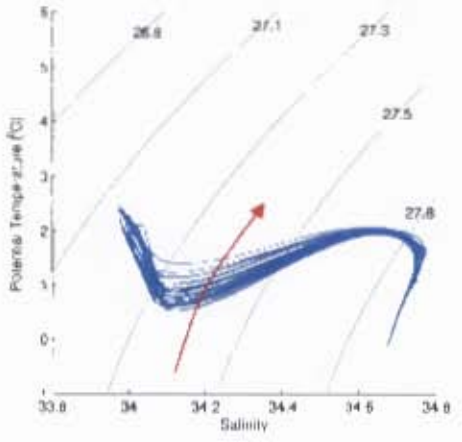

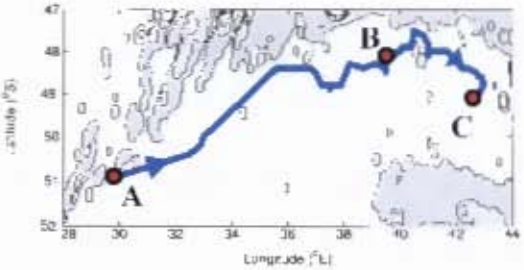

	Model Day	Lat (°S)	Lon (°E)
A	2300	50.9	29.8
B	2450	48.1	39.5
C	2600	49.1	42.6

Figure 7.2: Full-depth zonal sections across Eddy 5 at three positions, A, B and C, corresponding to when tracking started, during mid-life and when tracking ended. Top panel shows the potential temperature sections (contours at 0.5 °C intervals); Middle panel shows the salinity sections (contours at 0.1 psu interval between 33.5 and 34.5 and at 0.05 psu between 34.5 and 35); Bottom panel shows the meridional full-depth velocity v (contours at 10 cm s^{-1} intervals). The θ/S plot shows the decay in water mass – one profile taken at each time step at the core of the eddy. The track of Eddy 5 is also shown – the plot is similar to that shown in Figure 6.1 (pg 53). Arrows indicate the time line.

Eddy 5 was the longest-lasting feature (300 days or 10 months; April – February) to have travelled the greatest distance (1422 km) among the collection of 22 eddies tracked in chapter 6. Its average propagation speed of 4.74 km day^{-1} is below the overall mean. The locations A, B and C on the figure indicate the position at which sections were drawn. The distance covered by Eddy 5 between location A and B is 968 km, which is almost twice as much as the distance between B and C, over the same period of 5 months (150 model days). This particular eddy reached its maximum intensity 4 months after generation (Figure 7.1b) and remained roughly at that level of intensity (~ -47 cm) for about a month. In this case, maturity occurred in a region where other eddies usually dissipate, between 38 – 40°E. Uncharacteristically, it took a longer time to decay, lingering between the Del Caño and Conrad Rise. The θ/S profiles at the core of the eddy unmistakably characterises the eddy as of Antarctic origin. However, it is surprising that the eddy has undergone only a slight modification in water mass structure despite the distance covered and the slow translation. A close inspection of the vertical sections reveals some useful information. At the generation stage, Eddy 5 is recognisable by the shallow (~ 200 m) and wide (~ 175 km in diameter) layer of temperature minimum core and shoaling temperature and salinity isolines. The velocity structure shows a weak clockwise rotation, which a slightly stronger and more defined at its western edge. At maturity the eddy reaches a depth of about 2000 – 3000 m and the rotation is recognisable. Furthermore, the surface and sub-surface expression of the eddy are also very distinct from surrounding waters. At its final stage (position C), where tracking was terminated, the surface expression of the feature has been homogenised, to such extent as to making it difficult to be identified from its SST and SLA signatures. It is evident that the eddy, although weaker, is still present.

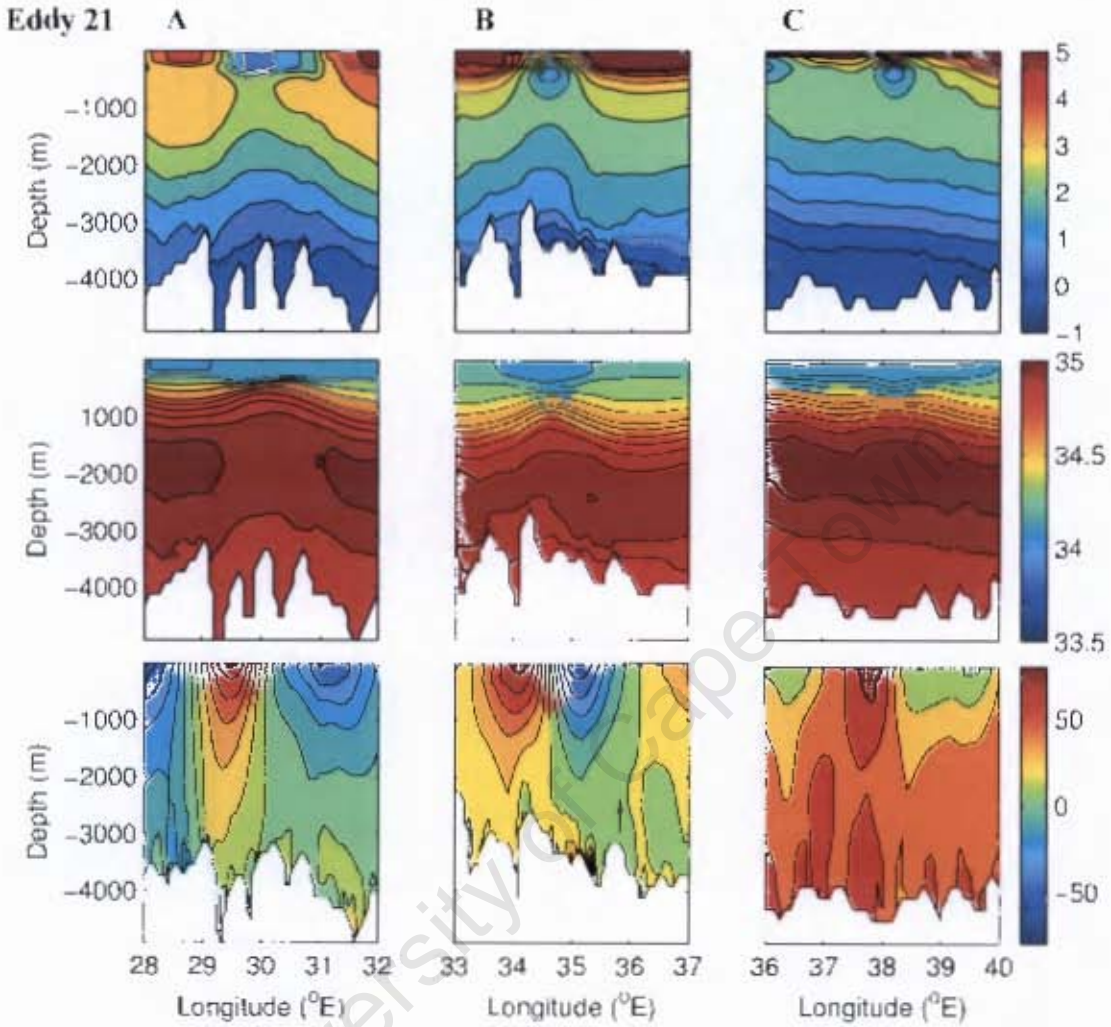

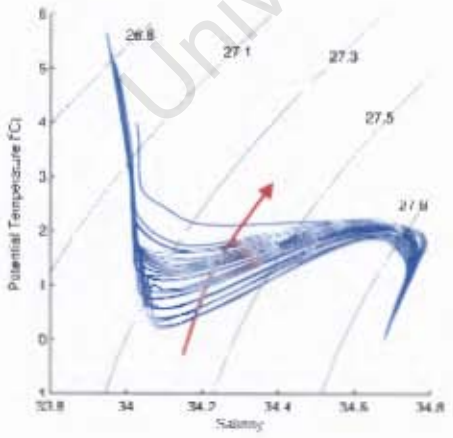

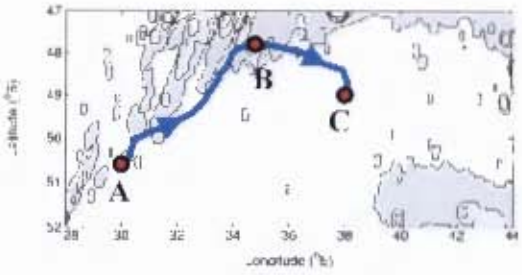

	Model Day	Lat (°S)	Lon (°E)
A	2105	50.6	30.0
B	2180	47.8	34.8
C	2220	49.0	38.0

Figure 7.3: Same as Figure 7.2, but for Eddy 21.

In contrast to the first eddy, Eddy 21 was short-lived, lasting only 115 days (October – January). Its translation speed of 7.06 km day^{-1} was however well above average and consequently it travelled a distance of 812 km. This particular eddy closely followed the f/h = 0.4 rad s^{-1} m^{-1} contour of the eastern flank of the SWIR between positions A and B. The steering influence of the ridge is illustrated in this case. It very rapidly reached its peak intensity (1 month after generation) and thereafter decayed gradually (Figure 7.1b). When tracking began, at position A, it is evident from the vertical section that the feature was not at the initial stage of development. In this case, the selection fields used to identify eddies failed to capture this feature at its inception. Water masses at the core of this eddy show significant modification throughout the water column, with a pronounced change in potential temperature of ~2 °C along the σ_0 = 27.3 isopycnal. At position C, the eddy had decayed almost completely. The remnant of the feature can only be identified in the potential temperature section with a central sub-surface minimum between ~200 and ~600 m. The isotherms as well as the isohalines below that level show relatively strong stratification. Furthermore, the velocity section shows that the rotation velocity dropped from >50 cm s^{-1} to ~10 cm s^{-1}.

Both eddies originated in the Antarctic Zone, roughly at 51°S; 30°E, with an SLA signature ~ -35 cm (Figure 7.1b). However, they differ in their character, trajectory, and decay. Eddy 21 travelled at a greater speed but shorter distance than Eddy 5. The peak intensity reached by both eddies were comparable. In the first case, it took Eddy 5 4 months (40% of its life) to reach its peak intensity. Thereafter, it underwent a slow and gradual decrease in SLA signature. In contrast, Eddy 21 only spent 1 month (25% of its life) to evolve fully and thereafter spun out relatively fast.

7.3. Conclusions.

Having assessed the OCCAM's depiction of the general mean circulation at the South-West Indian Ridge (chapter 5) and its representation of intense large-amplitude mesoscale eddies (chapter 6), this chapter dealt with the last question – how do eddies change over time? Owing to the lack of positive anomalies (warm eddies) fitting the criteria

(described in section 4.5.2) used to identify and track eddies within the model, only the 20 negative anomalies (cold eddies) tracked in chapter 6 have been used in this chapter to investigate and describe the process of eddy decay further.

Each individual eddy is manifestly different. Nevertheless, there are some similarities in their overall behaviour. Their trajectories generally follow the eastern flank of the SWIR, in an area between 48 – 50°S and 33 – 37°E. Intense eddies at the SWIR last on average 4 months (65% of eddies tracked) and are very rapidly re-absorbed into the mean flow (see also Table 3, pg 55). Very few eddies were observed persisting more than 7 months. Intense eddies were defined as |SLA| > 30 cm from Table 1. However, in most cases, (18 out of 20) eddies reached a peak SLA amplitude exceeding -40 cm. The time after generation to reach maximum intensity varied greatly amongst individual eddies. The decay of two eddies was studied in-depth. The degree of water mass decay was ostensibly linked to the advection speed of the features. Eddy 21 travelled at an above-average speed and underwent a pronounced decay through the water column. In contrast, with a slow propagation speed, Eddy 5 experienced very little water mass change. In both cases, the cyclonic rotation associated with the features also considerably weakened. However, the sub-surface temperature minimum core seemed to linger longer.

8. SUMMARY AND CONCLUSIONS.

Unusually high mesoscale activity in the Southern Ocean occurs in regions where the eastward flowing Antarctic Circumpolar Current interacts with the local topography. In the African sector of the Southern Ocean, the South-West Indian Ridge lies in a near-meridional position and directly influences the oceanographic environment of the Prince Edward Islands. Initial exploratory surveys around the archipelago were puzzling. Patches of zooplankton communities from the sub-tropics, the sub-antarctic and the antarctic were all observed in the vicinity of the islands. The abundant but transient availability of various plankton species help sustain a variety of top predators on the islands. The immediate interaction between ACC and the Prince Edward Islands was thought to be the reason for the enhanced biological activities observed. However, further large-scale hydrographic surveys and satellite products shed some light into this complex physical and biological setting. The vast and heterogeneous population of plankton close to the islands was also found to be linked to the dynamics occurring at the SWIR.

The instability induced on the ACC by the ridge system promotes the geneses of mesoscale eddies and thereby provides a mechanism for the meridional transport of organisms, water masses, heat and salt. The need to study eddies at the SWIR further became necessary and continuous monitoring of the features was needed. However, to repeatedly monitor eddies hydrographically is logistically impractical in that region due to the limited available ship time, the seasonal extent of the sea-ice and severe winter weather. Using numerical model outputs may therefore provide an insight into the dynamics of eddy generation, movement and ageing. This project explored the use of the $^{1}/_{4}^{o}$ (OC-4) and $^{1}/_{12}^{o}$ (OC-12) horizontal resolutions of the Ocean Circulation and Climate Advanced Modelling (OCCAM) outputs.

The main objective of this study was to assess the model outputs in a way that is pertinent to that region. This task has been carried out in two parts (first 2 key questions). Furthermore, in the final key question, the decay of two eddies identified within the model has been studied.

1. Does OCCAM reasonably depict the general circulation at the SWIR?

This project drew from a number of datasets to address this question. Using hydrographic sections available in that region, the model's representation of the two main frontal systems – the Subantarctic Front and the Antarctic Polar Front – were assessed. The SAF and APF were identified at 48°S and 50.3°S along a climatological section at 30°E drawn using OC-12 (OCCAM at $^1/_{12}^o$ horizontal resolution) outputs. Further east, along 40°E, the SAF was deflected north while the APF remained roughly at the same latitude, which effectively widened the Antarctic Polar Frontal Zone. In OC-4 ($^1/_4^o$ horizontal resolution), the SAF lay at 45°S and the APF at 50.4°S along the 30°E section. The mean sub-surface velocity from a comprehensive collection of drifting buoy data and eddy kinetic energy from satellite data were used for further comparisons between OC-4, OC-12 and observations. OCCAM underestimated the sub-surface velocities at both resolutions, but was qualitatively reasonably similar. The energy associated with the eddy flow (> 500 cm^{-2} s^{-2}) in OC-12 was comparable to that observed using altimetry data.

The larger-scale influence of the SWIR was also explored. A region of low sub-surface velocity and low eddy kinetic energy was identified centred at 53°S, 40°E, corresponding to the location of the Conrad Rise. Two high-velocity jets were observed north and south of the Rise. In the literature, very little is mentioned about the circulation around the Conrad Rise. Within the model, OC-4 poorly represented the jets. OC-12 outputs agreed fairly well with observations and showed the southern branch of the circulation to be slightly more energetic than the northern one. It was therefore proposed that the Conrad Rise may act as an obstruction to the flow of the Antarctic Circumpolar Current.

It was expected that OC-12 would be better at depicting the circulation at the SWIR than OC-4. Indeed, the variability observed at the ridge in OC-12 was very similar to that shown in altimetry. This conclusion strongly supported the decision to only use OC-12 to address the next question of looking at eddies at the SWIR.

2. Are intense mesoscale features generated within the model?

An important aspect of the project was the identification and tracking of eddies using successive sea level anomalies (SLA) maps from the model (OC-12) outputs. Because of the highly variable nature of the SWIR region, there was a need to distinguish between eddies and other by-products (such as meanders) of the variability. To this end, a method by Isern-Fontanet *et al.* (2003) was adopted. Using the horizontal velocity fields, a parameter Q was derived and used in conjunction with the SLA fields. Appropriate thresholds were applied to both fields and these were defined heuristically and through examples. Effectively, identification and monitoring of eddies were made simple and standard. Tracking of features were also undertaken in a standardised fashion following predefined rules: (1) only features originating in the region of the Andrew Bain fracture zone were considered; (2) focus was set on intense features ($|SLA| > 30$ cm) only; (3) tracking was maintained as long as the magnitude of the SLA exceeded 15 cm and $Q > 1 \times 10^{-10}$ s^{-2}. Results obtained were compared with a study undertaken by Ansorge and Lutjeharms (2003).

Twenty-two intense eddies were identified and tracked within the model over a 10-year period. After generation east of the Andrew Bain Fracture Zone, the features closely followed the $f/h = 0.4$ s^{-1} m^{-1} contour along the eastern flank of the ridge. On average, mesoscale eddies had longevities of 4.89 ± 2.20 months. With a mean translation speed of 5.51 ± 1.57 km day^{-1}, they covered a distance of 783 ± 303 km. These characteristic values were found to agree sufficiently with direct observations following a series of dedicated hydrographic surveys. In addition, the overall results agreeing well with Ansorge and Lutjeharms (2003) gave further confidence in the model.

A vertical zonal section through a typical model eddy and two θ/S profiles were drawn. This particular eddy was about 110 km in diameter and reached a depth of ~2500 m. The meridional velocities associated with the feature demarcated the eddy from its surrounding. Water masses at the core of the eddy were unquestionably of

antarctic origin and comparison made with a profile in the Antarctic Polar Frontal Zone illustrated the anomalous salt and heat content associated with the feature.

Of the 22 eddies tracked within the model, only 2 were warm. This was not expected since Ansorge and Lutjeharms (2003) have observed approximately the same number of positive and negative anomalies. Several possible reasons for this inconsistency were explored. It is very likely that the predefined tracking rules were too stringent and consequently hampered the identification of warm eddies within the model. Moreover, warm eddies are typically of sub-antarctic or sub-tropical origin and the likelihood of them being generated at the Andrew Bain Fracture Zone is slim and would largely depend on the variability in the location of the SAF. While the discrepancy could have been due to the choices made in this project, it is also possible that Ansorge and Lutjeharms might have overestimated the number of warm eddies. In particular, the identification and tracking of their anomalies were undertaken using slightly different criteria. The two warm eddies in the model were left out from further analysis.

3. **Given the reasonable representation of intense eddies within OCCAM at the SWIR, how do the features change with age?**

The twenty cold eddies identified within the model were further analysed to investigate how they change during their decay. It took approximately 1.5 – 2.5 months for an eddy to reach maximum intensity after generation between 30 – 32°E. In most cases, eddies underwent a dissipation period of 3 months after reaching peak intensity. Very few long-lived (>7 months) eddies were observed in the dataset. Decay was measured by the decrease in sea level anomaly (SLA) signatures of eddies, the weakening of their clockwise rotation as well as their anomalous temperature and salinity signatures relative to their surrounding.

Two eddies originating at the same location and starting with similar initial SLA signatures were examined closely. It was found that their behaviour and dissipation

rate differed considerably. In the first case, the eddy travelled slowly and reached its peak intensity 4 months after generation. Despite being long-lasting (10 months), it underwent very little water mass decay. Moreover, when tracking terminated, there was evidence that the weakened feature was still present 300 m below the surface. In contrast, the second eddy was fast moving and very rapidly reached maximum intensity. It had a more pronounced decay rate and consequently lasted only ~4 months. Water masses at the core of the eddy showed considerable modification. These two examples illustrated the distinctiveness of eddies at the South-West Indian Ridge.

Monitoring the genesis, movement and decay of features are deemed important for understanding the behaviour of seal, penguin and albatross colonies living on the Prince Edward Islands. The impact of eddies in that region reaches beyond the biology. The anomalous heat and salt content of these features being geographically relocated may contribute towards the climatic meridional exchange and balance of heat and salt in that region. Therefore, an accurate method of identification and tracking of eddies is required, without the need to hydrographically monitor each of them. The choice of SLA and Q thresholds in this project was defined partly by following the literature and partly through heuristic examples. The subjectiveness in determining these thresholds may have contributed to the apparent lack of warm eddies within OCCAM. Applying different thresholds for warm and cold eddies could have yielded better results.

The origins of these warm features are typically from the sub-antarctic or the sub-tropic and are therefore fundamentally different from cold eddies, whose origins are from the antarctic. A series of comprehensive hydrographic surveys of warm eddies at the South-West Indian ridge are required to understand their behaviour (see Ansorge *et al.*, submitted). In 2000, three successive cruises were undertaken to extensively monitor the evolution of a single Agulhas Ring – eddy Astrid (Van Veldhoven, 2005). Such a study is necessary at the SWIR. Moreover, in order to accomplish realistic results, the decay of both warm and cold eddies needs to be adequately incorporated within global ocean circulation models.

This project provided the opportunity for discovering another region in the Southern Ocean where the Antarctic Circumpolar Current is obstructed by a topographic feature. The shallow nature of the Conrad Rise appears to cause the ACC to bifurcate around it forming two high-velocity quasi-permanent jets. Currently, an investigation is underway to characterise this finding using several independent datasets (Durgadoo *et al.*, submitted). Moreover, a dedicated large-scale hydrographic survey is planned for April 2008 to systematically explore the area within its biogeochemical context.

Eddies at the South-West Indian Ridge undoubtedly warrant further studies. The high resolution global model, OCCAM, has proven to represent the circulation at the ridge with adequacy. Therefore, its outputs can now be used with reasonable confidence to further investigate the dynamics in that region. However, unfortunately OCCAM does not lend itself to sensitivity studies since the resources necessary to run an eddy-resolving ($^{1}/_{12}^{o}$) global ocean model are not available. The original intentions for this study were to determine how changes in the ACC flux and its associated frontal systems affect eddy generation at the South-West Indian Ridge. In the future, other models, such as NEMO (Madec, 2008) or ROMS (Shchepetkin and McWilliams, 2005) will be explored to investigate the sensitivity of eddy generation at the ridge.

ACKNOWLEDGEMENTS.

I am extremely grateful and fortunate to have had Dr Isabelle Ansorge as supervisor. Her friendly guidance and advice over the last two years were outstanding. The opportunities provided to me under her supervision made my MSc. experience a most interesting and rewarding one. I would also like to acknowledge Prof. Johann Lutjeharms for his mentorship and insightful reviews on drafts of this dissertation.

The main dataset used for this project was the OCCAM model outputs. These were acquired during a three months visit to the National Oceanography Centre, Southampton, UK. During that period, I was under the supervision of Mrs B.A. de Cuevas, who I would like to thank for helping me to understand the model dynamics. This trip was made financially possible by the University of Cape Town, the South African National Antarctic Programme (Miss C. Levieux) and the Social Science Research Council Mellon-Mays Graduate Initiative Program.

The secondary datasets used for this study were freely downloaded via http or ftp. Hydrographic data are available from the WOCE Hydrographic Program Office at http://woce.nodc.noaa.gov/woce_v3/wocedata_1/whp/. The drifter collection is obtainable from the Data Assembly Centre at the Atlantic Oceanographic and Metrological Laboratory at http://www.aoml.noaa.gov/phod/dac/dactata.html. Altimetry data, from AVISO, is accessible from ftp://ftp.cls.fr/pub/oceano/AVISO/SSH/duacs/global/dt/ref/msla/merged/. And lastly, AMSR-E data, produced by Remote Sensing Systems, are available at www.remss.com.

Finally, I would like to acknowledge the South African National Antarctic Programme and the University of Cape Town for their final support in the form of bursaries over the last two years.

May 2008.

REFERENCES.

Aksenov Y. (2002) – The sea ice-ocean global couple model ARCICE project report Part 1: description of dynamical thermodynamical sea ice model. *SOC Research and Consultancy Report No. 103.* 83 pp.

Allanson B.R., B.P. Boden, C.M. Duncombe Rae (1985) – A contribution to the oceanography of the Prince Edward Islands. In: Siegfried W.R., Condy P.R., Laws R.M. (eds) *Antarctic nutrient cycles and food webs.* Springer, Berlin Heidelberg 30–45 pp.

Ansorge I.J., P.W. Froneman, E.A. Pakhomov, J.R.E. Lutjeharms (1998) – Hydrographic and biological data report on the Marion Island Oceanographic Survey 2 (MIOS 2). *UCT Oceanography Report.* **98-1**.

Ansorge I.J., P.W. Froneman, E.A. Pakhomov, J.R.E. Lutjeharms, R. Perissinotto, R.C. van Ballegooyen (1999) – Physical-biological coupling in the waters surrounding the Prince Edward Islands (Southern Ocean). *Polar Biology.* **21**, 135–145.

Ansorge I.J. and J.R.E. Lutjeharms (2000) – Twenty-five years of physical oceanographic research at the Prince Edward Islands. *South African Journal Science.* **96**, 557–565.

Ansorge I.J. and J.R.E. Lutjeharms (2002) – The hydrography and dynamics of the ocean environment of the Prince Edward Islands (Southern Ocean). *Journal of Marine Systems.* **37**, 107–127.

Ansorge I.J. and J.R.E. Lutjeharms (2003) – Eddies originating at the South-West Indian Ridge. *Journal of Marine Systems.* **39**, 1–18.

Ansorge I.J., P.W. Froneman, J.R.E. Lutjeharms, K. Bernard, A. Bernard, L. Lange, D. Lukac, B. Backeburg, J. Blake, S. Bland, N. Burls, M. Davies-Coleman, R. Gerber, S. Gildenhuys, P. Hayes-Foley, A. Ludford, T. Manzoni, E. Robertson, S. Southey, S. Swart, D. Van Rensburg, S. Wynne (2004) – An interdisciplinary cruise dedicated to understanding ocean eddies upstream of the Prince Edward Islands. *South African Journal Science.* **100**, 319–322.

Ansorge I.J. and J.R.E. Lutjeharms (2005) – Direct observations of eddy turbulence at a ridge in the Southern Ocean. *Geophysical Research Letters.* **32**, L14603 doi: 10.1029/2005GL022588.

Ansorge I.J., J.R.E. Lutjeharms, N.C. Swart, J.V. Durgadoo (2006) – Observational evidence for a cross frontal heat pump in the Southern Ocean. *Geophysical Research Letters.* **33**, L19601 doi: 10.1029/2006GL026174.

Ansorge I.J., E.A. Pakhomov E.A., S. Kaehler, J.R.E. Lutjeharms, J.V. Durgadoo – Physical and biological coupling in eddies in the lee of the South-West Indian Ridge. *Deep-Sea Research.* submitted.

Arakawa A. (1966) – Computational design for long-term numerical integration of the equations of fluid motion: Two-dimensional incompressible flow, Part 1. *Journal of Computational Physics.* **1**, 119–143.

Belkin I.M. and A.L. Gordon (1996) – Southern Ocean fronts from the Greenwich meridian to Tasmania. *Journal of Geophysical Research.* **101**, 3675–3696.

Bernard K.S. and P.W. Froneman (2003) – Mesozooplankton community structure and grazing impact in the Polar Frontal Zone of the south Indian Ocean during austral autumn 2002. *Polar Biology.* **26**, 268–275, doi: 10.1007/s00300-002-0472-x.

Bernard A.T.F., I.J. Ansorge, P.W. Froneman, J.R.E. Lutjeharms, K.S. Bernard, N.C. Swart (2007) – Entrainment of Antarctic euphausiids across the Antarctic Polar Front by a cold eddy. *Deep-Sea Research I.* **54**, 1841–1851, doi: 10.1016/j.dsr.2007.06.007.

Best S.E., V.O. Ivchenko, K.J. Richards, R.D. Smith, R.C. Malone (1999) – Eddies in numerical models of the Antarctic Circumpolar Current and their influence on the mean flow. *Journal of Physical Oceanography.* **29**, 328–350.

Bleck R., S. Dean, S. Sun (1997) – Global ocean simulations with an isopycnic coordinate mode. In: *Some New Directions in Science on Computers.* 297–317. World Science, River Edge, N.J.

Boden B.P. (1988) – Observations of an island mass effect in the Prince Edward Archipelago. *Polar Biology.* **9**, 1–8.

Bryan K. (1969) – A numerical method for the study of the circulation of the world ocean. *Journal of Computational Physics.* **4**, 347–376.

Budillon G. and S.R. Rintoul (2003) – Fronts and upper ocean thermal variability south of New Zealand. *Antarctic Science.* **15**, 141–152.

Coward A.C., P.D. Killworth, J.R. Blundell (1994) – Tests of a two-grid world ocean model. *Journal of Geophysical Research.* **99**, 22725–22735.

Coward A.C. and B.A. de Cuevas (2005) – The OCCAM 66 level model: physics, initial conditions and external forcing. *SOC Internal Document No 99.* 58 pp.

Cox M.D. (1984) – A primitive equation 2-dimensional model of the ocean. *GFDL Technical Report No 1.* Geophysical Fluid Dynamics Laboratory/NOAA, Princeton University, N.J. 08542, USA 143 pp.

Craneguy P. and Y.-H. Park (1999) – Contrôle topographique du courant circumpolaire antarctique dans l'océan Indien de sud. *Compte Rendu Académie des Sciences, Science de la terre et de planètes.* **328**, 583–589.

Cunningham S.A., G. Alerson, B.A. King, M.A. Brandon (2003) – Transport and variability of the Antarctic Circumpolar Current in Drake Passage. *Journal of Geophysical Research.* **108**, 8084, doi: 10.1029/2001JC001147.

DBDB5 (1983) – U.S. Naval Oceanographic Office, and the U.S. Naval Ocean Research and Development Activity. U.S.N.O.O., Bay St Louis, Mississippi.

de Szoeke R. and M. Levine (1981) – The advective flux of heat by mean geostrophic motions in the Southern Ocean. *Deep-Sea Research.* **28**, 1057–1085.

Döös K. and D.J. Webb (1994) – The Deacon cell and the other meridional cells of the Southern Ocean. *Journal of Physical Oceanography.* **24**, 429–442.

Drijfhout S.S., P. de Vries, K. Döös, A.C. Coward (2003) – Impact of eddy-induced transport on the lagrangian structure of the upper branch of the thermohaline circulation. *Journal of Physical Oceanography.* **33**, 2141–2155.

Ducet N., P.Y. Le Traon, G. Reverdin (2000) – Global high-resolution mapping of ocean circulation from TOPEX/Poseidon and ERS-1 and -2. *Journal of Geophysical Research.* **105**, 19477–19498.

Duncombe Rae C.M. (1989a) – Frontal systems encountered between southern Africa and the Prince Edward Islands during April/May 1987. *South African Journal of Antarctic Research.* **19**, 21–25.

Duncombe Rae C.M. (1989b) – Physical and chemical marine environment of the Prince Edward Islands (Southern Ocean) during April/May 1987. *South African Journal of Marine Science.* **8**, 301–311.

Duncombe Rae C.M. (1989c) – Data report of the first cruise of the Marion Off-shore Ecological study (MOES-I). *Rep. South African Natural Scientist Programs.* **159**, 384 pp.

Durgadoo J.V., J.R.E. Lutjeharms, A. Biastoch, I.J. Ansorge – The Conrad Rise as an obstruction to the Antarctic Circumpolar Current. *Geophysical Research Letters.* submitted.

Froneman P.W., I.J. Ansorge, E.A. Pakhomovo, J.R.E. Lutjeharms (1999) – Plankton community structure in the physical environment surrounding the Prince Edward Islands (Southern Ocean). *Polar Biology.* **22**, 145–155.

Froneman P.W., I.J. Ansorge, L. Vumazonke, M.K. Gulekana, K. Bernard, A.M. Webb, W. Leukes, C.M. Risien, S. Thomalla, J. Hermes, M. Knott, D. Anderson, N. Hargey, M. Jennings, J. Veitch, J.R.E. Lutjeharms, C.D. McQuaid (2002) – Physical and biological variability in the Antarctic Polar Frontal Zone: report on research cruise 103 of the MV SA Agulhas. *South African Journal of Science.* **98**, 534–536.

Gairola R.M., S.K. Basu, P.C. Pandey (2001) – Eddy detection over Southern Indian Ocean using TOPEX/POSEIDON altimeter data. *Marine Geodesy.* **24**, 107–121.

Gent P.R. and J.C. McWilliams (1990) – Isopycnal mixing in ocean circulation models. *Journal of Physical Oceanography.* **20**, 150–155.

Gille S.T. (2002) – Warming in the Southern Ocean since the 1950s. *Science.* **295**, 1275–1277.

Gordon H.B. and S.P. O'Farrell (1997) – Transient climate change in the CSIRO coupled model with dynamical sea ice. *Monthly Weather Reviews.* **125**, 875–907.

Gouretski V.V. and A.I. Danilov (1993) – Weddell Gyre: structure of the eastern boundary. *Deep-Sea Research I.* **40**, 561–582.

Hirst A.C. (1999) – The Southern Ocean response to global warming in the CSIRO coupled ocean-atmosphere model. *Environmental Modelling and Software.* **14**, 227–241.

Holliday N.P. and J.F. Read (1998) – Surface oceanic fronts between Africa and Antarctica. *Deep Sea Research I.* **45**, 217–238.

Hughes C.W. and E.R. Ash (2001) – Eddy forcing of the mean flow in the Southern Ocean. *Journal of Geophysical Research.* **106**, 2713–2722.

Isern-Fontanet J., E. Garcia-Ladona, J. Font (2003) – Indentification of marine eddies from altimetric maps. *Journal of Atmospheric and Oceanic Technology.* **20**, 772–778.

Jakobsson M., N.Z. Cherkis, J. Woodward, R. Macnab, B. Coakley (2000) – New grid of Arctic bathymetry aids scientists and mapmakers. *EOS, Transaction of the American Geophysical Union.* **81**, 89.

Jeong J., F. Hussain, J. Font (1995) – On the identification of a vortex. *Journal of Fluid Mechanics.* **285**, 69–94.

Jonker F.C., M.N. Bester (1998) – Seasonal movements and foraging areas of adult southern female elephant seals, Mirounga leonina, from Marion Island. *Antarctic Science.* **10**, 21–30.

Joyce T.M., S.L. Patterson, R.C. Millard (1981) – Anatomy of a cyclonic ring in the Drake Passage. *Deep-Sea Research.* **28**, 1265–1287.

Kalnay E., M. Kanamitsu, R. Kistler, W. Collins, D. Deaven, L. Gandin, M. Iredell, S. Saha, G. White, J. Woollen, Y. Zhu, M Chelliah, W. Ebisuzaki, W. Higgins, J. Janawiak, K.C. Mo, C. Ropelewskia, A. Leetmaa, R. Reynolds, R. Jenne (1996) – The NCEP/NCAR reanalysis project. *Bulletin of the American Meteorological Society.* **77**, 437–495.

Killworth P.D., D. Stainforth, D.J. Webb, S.M. Paterson (1991) – The development of a free surface Bryan-Cox-Semtner ocean model. *Journal of Physical Oceanography.* **21**, 1333–1348.

Koshlyakov M.N., Y.M. Grachev, T.G. Sazhina, M.I. Yaremchuk (1985) – A cyclonic eddy in the Antarctic Circumpolar Current and heat transport across the Antarctic Front. *Oceanology.* **25**, 685–691.

Kostianoy A.G., A.I. Ginzburg, M. Frankignoulle, B. Delille (2004) – Fronts in the Southern Indian Ocean as inferred from satellite sea surface temperature data. *Journal of Marine Systems.* **45**, 55–73.

Large W.G., J.C. McWilliams, S.C. Doney (1994) – Ocean vertical mixing: A review and a model with a nonlocal boundary layer parameterisation. *Reviews of Geophysics.* **32**, 363–403.

Le Traon P.Y., F. Nadal, N. Ducet (1998) – An improved mapping method of multi-satellite altimeter data. *Journal of Atmospheric and Oceanic Technology.* **15**, 522–534.

Lee M.-M., A.C. Coward, A.J.G. Nurser (2002) – Spurious diapycnal mixing of the deep waters in an eddy-resolving global ocean model. *Journal of Physical Oceanography.* **32**, 1522–1535.

Lee M.-M. and A.C. Coward (2003) – Eddy mass transport for the Southern Ocean in an eddy-permitting global ocean model. *Ocean Modelling.* **5**, 249–266.

Lee M.-M., A.J.G. Nurser, A.C. Coward, B.A. de Cuevas (2007) – Eddy advective and diffusive transports of heat and salt in the Southern Ocean. *Journal of Physical Oceanography.* **37**, 1376–1393.

Legeais J-F., S. Speich, M. Arhan, I.J. Ansorge, E. Fahrbach, S. Garzoli, A. Klepikov (2005) – The baroclinic transport of the Antarctic Circumpolar Current south of Africa. *Geophysical Research Letters.* **32**, L24602 doi: 10.1029/2005GL023271.

Leonard B.P. (1979) – A stable and accurate convective modelling procedure based on quadratic upstream interpolation. *Computational Method of Applied Mechanical Engineering.* **19**, 59–98.

Levitus, S., T.P. Boyer, M.E. Conkright, T. O'Brien, J. Antonov, C. Stephens, L. Stathoplos, D. Johnson, R. Gelfeld (1998) – *World Ocean Database 1998* Volume 1: Introduction. NOAA Atlas NESDIS 18, U.S. Government Printing Office, Washington, D.C.

Lutjeharms J.R.E. and H.R. Valentine (1984) – Southern Ocean thermal fronts south of Africa. *Deep-Sea Research.* **31**, 1461–1475.

Lutjeharms J.R.E. (1985) – Location of frontal systems between Africa and Antarctica: some preliminary results. *Deep-Sea Research.* **32**, 1499–1509.

Lutjeharms J.R.E. (1990) – Temperatuurstruktuur van die oseaanbolaag tussen Kaapstad en Marion-eiland. *South African Journal of Antarctic Research.* **20**, 21–32.

Lutjeharms J.R.E., S. Jamaloodien, I.J. Ansorge (2002) – The temporal displacement of ocean fronts south-east of Africa. *South African Journal Science.* **98**, 304–306.

Madec G. (2008) –NEMO reference manual, ocean dynamics component: NEMO-OPA. Preliminary version. *Note du Pole de modélisation, Institut Pierre-Simon Laplace (IPSL), France No 27*, ISSN No1288-1619, in press.

Maltrud M.E., R.D. Smith, A.J. Semtner, R.C. Malone (1998) – Global eddy-resolving ocean simulations driven by 1985-1995 atmospheric winds. *Journal of Geophysical Research.* **103**, 30825–30853.

Marsh R., A.J.G. Nurser, A.P. Megann, A.L. New (2000) – Water mass transformation in the Southern Ocean of a global isopycnal coordinate GCM. *Journal of Physical Oceanography.* **30**, 1013–1045.

Marti O., G. Madec, P. Delecluse (1992) – Comment on "Net diffusivity in ocean general circulation models with nonuniform grids" by F.L. Yin and I.Y. Fung. *Journal of Geophysical Research.* **97**, 12763–12766.

McQuaid C.D. and P.W. Froneman (2004) – The Southern Ocean Group at Rhodes University: seventeen years of biological oceanography in the Southern Ocean reviewed. *South African Journal Science.* **100**, 571–577.

Mélice J.-L., J.R.E. Lutjeharms, M. Rouault, I.J. Ansorge (2003) – Sea-surface temperatures at the sub-Antarctic islands Marion and Gough during the past 50 years. *South African Journal Science.* **99**, 1–4.

Mesinger F. and A. Arakawa (1976) – Numerical methods used in atmospheric models. *GARP Publication series No 17.* World Meteorological Organisation, Geneva, 64 pp.

Morrow R., F. Birol, D. Griffin, J. Sudre (2004a) – Divergent pathways of cyclonic and anti-cyclonic ocean eddies. *Geophysical Research Letters.* **31**, L24311, doi: 10.1029/2004GL020974.

Morrow R., J.R. Donguy, A. Chaigneau, S.R. Rintoul (2004b) – Cold-core anomalies at the Subantarctic front, south of Tasmania. *Deep-Sea Research I.* **51**, 1417–1440.

Nel D.C., J.R.E. Lutjeharms, E.A. Pakhomov, I.J. Ansorge, P.G. Ryan, N.T.W. Klages (2001) – Exploitation of mesoscale oceanographic features by grey-headed albatross

Thalassarche chrysostoma in the southern Indian Ocean. *Marine Ecology Progress Series.* **217**, 15–26.

Niiler P.P. and A.R. Robinson (1967) – The theory of free inertial jet. *Tellus.* **19**, 601–619.

Nowlin W.D. Jr and J.M. Klinck (1986) – The physics of the Antarctic Circumpolar Current. *Rev. Geophys.* **24**, 469–491.

Orsi A.H., T. Whitworth, W.D Nowlin (1995) – On the meridional extent and fronts of the Antarctic Circumpolar Current. *Deep-Sea Research I.* **42**, 641–673.

Pacanowski R.C. and S.G.H. Philander (1981) – Parameterisation of vertical mixing in numerical models of tropical oceans. *Journal of Physical Oceanography.* **11**, 1443–1451.

Pacanowski R.C. and A. Gnanadesikan (1998) – Transient response in a z-level ocean model that resolves topography with partial cells. *Monthly Weather Reviews.* **126**, 3248–3270.

Pacanowski R.C. K. Dixon, A. Rosati (1990) – The GFDL Modular Ocean Model user guide. *Technical Report No 2.* GFDL Ocean Group.

Pakhomov E.A. and C.D. McQuaid (1996) – Distribution of surface zooplankton and seabirds across the Southern Ocean. *Polar Biology.* **16**, 271–286.

Pakhomov E.A., I.J. Ansorge, P.W. Froneman (1998) – Prince Edward Islands' offshore oceanographic study: report of research cruise April-May 1997. *South African Journal of Science.* **94**, 153–156.

Pakhomov E.A., I.J. Ansorge, P.W. Froneman (2000a) – Variability in the inter-island environment of the Prince Edward Islands (Southern Ocean). *Polar Biology.* **23**, 593–603.

Pakhomov E.A., P.W. Froneman, I.J. Ansorge, J.R.E. Lutjeharms (2000b) – Temporal variability in the physico-biological environment of the Prince Edward Islands (Southern Ocean). *Journal of Marine Systems.* **26**, 75–95.

Pakhomov E.A., I.J. Ansorge, S. Kaehler, L.U. Vumazonke, K. Gulekana, T. Bushula, C. Balt, D. Paul, N. Hargey, H. Stewart, N. Chang, L. Furno, S. Mkatshwa, C. Visser, J.R.E. Lutjeharms, P. Hayes-Foley (2003) – Studying the impact of ocean eddies on the ecosystem of the Prince Edward Islands: DEIMEC II. *South African Journal Science.* **99**, 187–190.

Park Y-H., L. Gamberoni and E. Charriaud (1993) – Frontal structure, water masses and circulation in the Crozet Basin. *Journal of Geophysical Research.* **98**, 12361–12385.

Park Y.-H. and E. Charriaud (1997) – Hydrographic and baroclinic transport between Africa and Antarctica on WHP Section I6. *International WOCE Newsletter.* **29**, 13–16.

Park Y.-H., E. Charriaud, M. Fieux (1998) – Thermohaline structure of the Antarctic Surface Water / Winter Water in the Indian sector of the Southern Ocean. *Journal of Marine Systems.* **17**, 5–23.

Park Y.-H., E. Charriaud, P. Craneguy, A. Kartavtseff (2001) – Fronts, transport, and Weddell Cyre at 30°E between Africa and Antarctica. *Journal of Geophysical Research.* **106**, 2857–2879.

Pawlowicz R. (2006) – M_map: A mapping package for Matlab. http://www.eos.ubc.ca/~rich/map.html

Perissinotto R. and B.P. Boden (1989) – Zooplankton-phytoplankton relationships at the Prince Edward Islands during April/May 1995 and 1986. *South African Journal of Antarctic Research.* **19**, 26–30.

Perissinotto R., C.M. Duncombe Rae, B.P. Boden, B.R. Allanson (1990) – Vertical stability as a controlling factor of the marine phytoplankton production at the Prince Edward Archipelago (Southern Ocean).*Marine Ecology Progress Series.* **60**, 205–209.

Perissinotto R. and C.M. Duncombe Rae (1990) – Occurrence of anti-cyclonic eddies on the Prince Edward Plateau (Southern Ocean): effects on phytoplankton biomass and production. *Deep-Sea Research.* **37**, 777–793.

Perissinotto R., J.R.E. Lutjeharms, R.C. van Ballegooyen (2000) – Biological-physical interactions and pelagic productivity at the Prince Edward Islands, Southern Ocean. *Journal of Marine Systems.* **24**, 327–341.

Pollard R.T., J.F. Read *et al.* (1994) – RSS Discovery Cruise 201, 23 Mar – 03 May 1993. South West Indian Ocean Experiment (SWINDEX). *Institute of Oceanographic Sciences Deacon Laboratory, Cruise Report.* **240**, 96 pp.

Pollard R.T. and J.F. Read (1997) – Two-year long current time series from the Southwest Indian Ocean. *International WOCE Newsletter.* **29**, 3–7.

Pollard R.T. and J.F. Read (2001) – Circulation pathways and transports of the Southern Ocean in the vicinity of the Southwest Indian Ridge. *Journal of Geophysical Research.* **106**, 2881–2898.

Read J.F. and R.T. Pollard (1993) – Structure and transport of the Antarctic Circumpolar Current and Agulhas Return Current at 40°E. *Journal of Geophysical Research.* **98**, 12281–12295.

Rintoul S.R. and S. Sokolov (2001) – Baroclinic transport variability of the Antarctic Circumpolar Current south of Australia (WOCE repeat section SR3). *Journal of Geophysical Research.* **106**, 2815–2832.

Rossow W.B. and R.A. Schiffer (1991) – ISCCP Cloud data products. *Bulletin of the American Meteorological Society.* **72**, 2–20.

Rouault M., J.-L. Mélice, C.J.C. Reason, J.R.E. Lutjeharms (2005) – Climate variability at Marion Island, Southern Ocean, since 1960. *Journal of Geophysical Research.* **110**, C05007 doi: 10.1029/2004JC002492.

Sandwell D.T. and W.H.F. Smith (1995) – Marine gravity from satellite altimetry. The geological data centre, Scripps Institute of Oceanography, La Jolla, CA 92093 (digital file, version 7.2) anonymous ftp to baltica.ucsd.edu.

Schlitzer R., Ocean Data View, http://www.awi-bremerhaven.de/GEO/ODV, 2007.

Semtner A.J. (1974) – A general circulation model for the World Ocean. *Technical report No 9.* Department of Meteorology, University of California, Los Angeles, 99 pp.

Semtner A.J. (1976) – A model for the thermodynamic growth of sea ice in numerical investigations of climate. *Journal of Physical Oceanography.* **6**, 379–389.

Semtner A.J. and R.M. Chervin (1988) – A simulation of the global ocean circulation with resolved eddies. *Journal of Geophysical Research.* **93**, 15502–15522.

Shchepetkin A. and J.C. McWilliams (2005) – The Regional Oceanic Modeling System: A split-explicit, free-surface, topography-following-coordinate ocean model. *Ocean Modelling.* **9**, 347–404.

Sinha B. and A. Yool (2006) – Extension of the OCCAM 1° ocean general circulation model to include the biogeochemical cycles of carbon and oxygen Part 1: Technical description. *SOC Research and Consultancy Report No. 5.* 80 pp.

Spencer R.W. (1993) – Global oceanic precipitation from the MSU during 1979-91 and comparisons to other climatologies. *Journal of Climate.* **6**, 1301–1326.

SSALTO/DUACS (2006) – SSALTO/DUACS user handbook: (M)SLA and (M)ADT near-real time and delayed time products. Version 1rev5. Ref: CLS-DOS-NT-06.034.

Stammer D. (1998) – On eddy characteristics, eddy transports, and mean flow properties. *Journal of Physical Oceanography.* **28**, 727–739.

Swart N.C., I.J. Ansorge, J.R.E. Lutjeharms (2008) – Detailed characterisation of an Antarctic eddy in the subantarctic. *Journal of Geophysical Research.* **113**, C01009 doi:10.1029/2007JC004190

The FRAM Group (Webb D.J. *et al.*) (1991) – An eddy-resolving model of the Southern Ocean. *EOS, Transactions of the American Geophysical Union.* **72**, 169–174.

Thorpe S.E., K.J. Heywood, M.A. Brandon, D.P. Stevens (2002) – Variability of the southern Antarctic Circumpolar Current front north of South Georgia. *Journal of Marine Systems.* **37**, 87–105.

Van Veldhoven A.K. (2005) – Observations of the evolution of Agulhas Rings. *PhD Thesis*. Royal Netherlands Institute for Sea Research (NIOZ) on Texel, the Netherlands.

Ward P., M. Whitehouse, M. Meredith, E. Murphy, R. Shreeve, R. Korb, J. Watkins, S. Thorpe, S. Grant, D. Bone (2002) – The Southern Antarctic Circumpolar Current Front: physical and biological coupling at South Georgia. *Deep-Sea Research.* **49**, 2183–2202.

Webb D.J., P.D. Killworth, A.C. Coward, S.R. Thompson (1991) – The FRAM Atlas of the Southern Ocean. Natural Environment Research Council, Swindon. 67pp.

Webb D.J. (1996) – An ocean model for array processor computers. *Computers and Geosciences.* **22**, 569–578.

Webb D.J., B.A. de Cuevas, A.C. Coward (1998a) – The first main run of the OCCAM global ocean model. *SOC Internal Document No 34.* 44 pp.

Webb D.J., B.A. de Cuevas, C.S. Richmond (1998b) – Improved advection schemes for ocean models. *Journal of Atmospheric and Oceanic Technology.* **15**, 1171–1187.

Weimerskirch H., P. Inchausti, C. Guinet, C. Barbraud (2003) – Trends in bird and seal populations as indicators of a system shift in the Southern Ocean. *Antarctic Science.* **15**, 249–256 doi: 10.1017/S0954102003001202.

Wells N. and B.A. de Cuevas (1995) – Depth-integrated vorticity budget of the Southern Ocean from a general circulation model. *Journal of Physical Oceanography.* **25**, 2569–2582.

Whitworth T. (1983) – Monitoring the transport of the Antarctic Circumpolar Current at Drake Passage. *Journal of Physical Oceanography.* **13**, 2045–2057.

Whitworth T. and R.G. Peterson (1985) – Volume transport of the Antarctic Circumpolar Current from bottom pressure measurements. *Journal of Physical Oceanography.* **5**, 810–816.

Whitworth T. and W.D. Nowlin (1987) – Water masses and currents of the Southern Ocean at the Greenwich meridian. *Journal of Geophysical Research.* **92**, 6462–6476.

Williams R.G. (1988) – Modification of ocean eddies by air-sea interaction. *Journal of Geophysical Research.* **93**, 15523–15533.

WOCE-SVP report No.1 (1988) – *WOCE/TOGA Surface Velocity Programme planning committee*. Report of the first meeting. NOAA AOML, Miami, Florida April 1988.
Xie P. and P.A. Arkin (1996) – Analyses of global monthly precipitation using gauge observations, satellite estimates and numerical model predictions. *Journal of Climate.* **9**, 840–858.

Yaremchuck M.I., N.L. Bindoff, J. Schröter, D. Nechaev, S.R. Rintoul (2001) – On the zonal and meridional circulation and ocean transports between Tasmania and Antarctica. *Journal of Geophysical Research.* **106**, 2795–2814.